

WISDOM Project - XVI. The link between circumnuclear molecular gas reservoirs and active galactic nucleus fuelling

Jacob S. Elford¹,¹★ Timothy A. Davis¹,¹ Ilaria Ruffa¹,¹ Martin Bureau,² Michele Cappellari¹,²
 Jindra Gensior³,³ Satoru Iguchi⁴,^{4,5} Fu-Heng Liang²,² Lijie Liu^{6,7},^{6,7} Anan Lu⁸
 and Thomas G. Williams²

¹Cardiff Hub for Astrophysics Research & Technology, School of Physics & Astronomy, Cardiff University, Queens Buildings, The Parade, Cardiff, CF24 3AA, UK

²Sub-department of Astrophysics, Department of Physics, University of Oxford, Denys Wilkinson Building, Keble Road, Oxford OX1 3RH, UK

³Institute for Computational Science, University of Zürich, Winterthurerstrasse 190, CH-8057 Zürich, Switzerland,

⁴Department of Astronomical Science, SOKENDAI (The Graduate University of Advanced Studies), Mitaka, Tokyo 181-8588, Japan

⁵National Astronomical Observatory of Japan, National Institutes of Natural Sciences, Mitaka, Tokyo 181-8588, Japan

⁶Cosmic Dawn Center (DAWN), Rådmandsgade 64, DK-2200 København N, Denmark

⁷DTU-Space, Technical University of Denmark, Elektrovej 327, DK-2800 Kgs. Lyngby, Denmark

⁸McGill Space Institute and Department of Physics, McGill University, 3600 rue University, Montreal, QC H3A 2T8, Canada

Accepted 2023 December 21. Received 2023 November 22; in original form 2022 December 10

ABSTRACT

We use high-resolution data from the millimetre-Wave Interferometric Survey of Dark Object Masses (WISDOM) project to investigate the connection between circumnuclear gas reservoirs and nuclear activity in a sample of nearby galaxies. Our sample spans a wide range of nuclear activity types including radio galaxies, Seyfert galaxies, low-luminosity active galactic nuclei (AGN) and inactive galaxies. We use measurements of nuclear millimetre continuum emission along with other archival tracers of AGN accretion/activity to investigate previous claims that at, circumnuclear scales (< 100 pc), these should correlate with the mass of the cold molecular gas. We find that the molecular gas mass does not correlate with any tracer of nuclear activity. This suggests the level of nuclear activity cannot solely be regulated by the amount of cold gas around the supermassive black hole (SMBH). This indicates that AGN fuelling, that drives gas from the large-scale galaxy to the nuclear regions, is not a ubiquitous process and may vary between AGN type, with time-scale variations likely to be very important. By studying the structure of the central molecular gas reservoirs, we find our galaxies have a range of nuclear molecular gas concentrations. This could indicate that some of our galaxies may have had their circumnuclear regions impacted by AGN feedback, even though they currently have low nuclear activity. Alternatively, the nuclear molecular gas concentrations in our galaxies could instead be set by secular processes.

Key words: galaxies: ISM – galaxies: active – galaxies: nuclei.

1 INTRODUCTION

It has been established that a supermassive black hole (SMBH) exists at the centre of almost all massive galaxies ($M_* \gtrsim 10^{9.5} M_\odot$). A large number of studies have shown that tight correlations exist between the masses of such SMBHs and the properties of their host galaxies (such as the bulge mass: e.g. Magorrian et al. 1998; Marconi & Hunt 2003 and velocity dispersion: e.g. Ferrarese & Merritt 2000; Tremaine et al. 2002; Gültekin et al. 2009), suggesting a self-regulated co-evolution between them (see e.g. Kormendy & Ho 2013 for a review). There is evidence that active galactic nuclei (AGN) and the associated energetic output can play a crucial role in setting up and maintaining SMBH-host galaxy co-evolution, as it can change the physical conditions of the surrounding interstellar medium (ISM) and/or expel it from the nuclear regions (e.g. Bower

et al. 2006; Croton et al. 2006; King & Pounds 2015; Harrison 2017; Morganti 2017). The many details of these processes, however, are still poorly understood.

In the local universe ($z < 0.1$), the AGN population can be separated into two main (non-exclusive) groups, differentiated by the mode of dominant energetic output: radiative and kinetic (e.g. Heckman & Best 2014). In the former the accretion occurs at high rates ($\gtrsim 1$ per cent of the Eddington limit) through optically thick and geometrically thin discs (Shakura & Sunyaev 1973). This mode is radiatively efficient, so the dominant energy output is from the conversion of the potential energy of the matter accreted onto each SMBH into electromagnetic radiation. Kinetic-mode AGN instead produce little radiation and channel the bulk of the energy generated from the accretion process into collimated outflows of non-thermal plasma (i.e. radio jets). In these objects the geometrically thin accretion disc is absent or truncated at some inner radii and likely replaced by geometrically thick, optically thin advection-dominated accretion flows (i.e. ADAFs; Narayan & Yi 1995), whereby the

* E-mail: elfordj@cardiff.ac.uk

material is accreted onto the SMBH at low rates ($\ll 1$ per cent of the Eddington limit).

Nearby radiative-mode AGN with weak or no radio jet emission have historically been called Seyfert galaxies. These objects possess all the characteristics of the ‘conventional’ AGN described in the framework of the standard unified model (e.g. Antonucci 1993; Urry & Padovani 1995), and are typically hosted by late-Hubble type galaxies (e.g. Martini et al. 2003). AGN producing strong kinetic feedback are instead typically identified as radio galaxies (RGs) and – based on their optical spectra – can be divided into two main classes (e.g. Best & Heckman 2012): high-excitation radio galaxies (HERGs) and low-excitation radio galaxies (LERGs). The former show strong high-ionization (Seyfert-like) emission lines in their optical spectra, produce both radiative and kinetic AGN feedback, and are typically hosted by massive ($M_* \gtrsim 10^{9.5} M_\odot$) early-type galaxies (ETGs). LERGs show no or weak, LINER (low-ionization nuclear emission-line region)-like emission lines in their optical spectra, produce almost exclusively kinetic feedback, and are typically found in very massive ($M_* \gtrsim 10^{11} M_\odot$) ETGs. Understanding the source of SMBH fuelling in the AGN populations introduced earlier is crucial to putting constraints on the physical processes driving and regulating the SMBH-host galaxy co-evolution. Up to now, however, a general picture for the fuelling of active SMBHs in the local universe is still missing.

The central regions of Seyfert galaxies have been often observed to be dominated by cold atomic and molecular gas (e.g. Combes et al. 2013; García-Burillo et al. 2014), suggesting a potential connection with their nuclear activities. The finding by Izumi, Kawakatu & Kohno (2016) of a positive correlation between the mass of ≈ 100 pc-scale circumnuclear discs (CNDs) of dense molecular gas and the black hole mass-accretion rate in nearby Seyferts seems to support this hypothesis. More recently, García-Burillo et al. (2021) also found that nuclear activity in these objects can cause deficits in their circumnuclear molecular gas reservoirs, with a negative trend between nuclear 2–10 keV X-ray luminosity and the central gas concentration. In both cases, however, the studies have been conducted on small samples of about 10 AGN of the same type. These samples also span relatively small ranges of AGN luminosities ($L_{2-10\text{keV}} \sim 10^{41} - 10^{44} \text{ erg s}^{-1}$) and host galaxy properties (almost exclusively barred spirals). It is therefore currently not clear whether or not the inferred cold gas–nuclear activity connection would hold over a broader population of active galaxies.

Alternatively, a long-established scenario suggests that the HERG/LEERG dichotomy may be a consequence of different sources for the accreting gas. In this framework, HERGs are fuelled at relatively high rates by cold gas acquired from merging or collisions with gas-rich galaxies (e.g. Best & Heckman 2012). LERGs are instead powered by the accretion of hot gas from the intergalactic medium (IGM) through Bondi spherical accretion (Bondi 1952; Hardcastle, Evans & Croston 2007). This hypothesis was initially supported by studies finding a correlation between jet power and Bondi accretion rate in LERGs (e.g. Allen et al. 2006; Hardcastle et al. 2007; Balmaverde, Baldi & Capetti 2008). Over the past decade, however, strong evidence has been acquired that cold gas can also play a role in fuelling LERGs, as large masses of cold gas and dust have been often observed at the centres of these objects (i.e. $M_{\text{H}_2} \sim 10^7 - 10^{10} M_\odot$; Ocaña Flaquer et al. 2010; Prandoni et al. 2010; North et al. 2019; Ruffa et al. 2019a, b, 2020). The total molecular gas mass of a sample of nearby ETGs (most of which are LERG hosts) have also been observed to weakly correlate with the AGN jet power, providing further evidence that there could be a close connection between the two (Babyk et al. 2019). Models

for cold gas SMBH fuelling in typical LERG hosts have been also developed and imply that the observed cold gas reservoirs originate from cooling of the hot X-ray emitting surrounding haloes, either directly and smoothly (e.g. Negri et al. 2014) or after chaotic cooling (as predicted in chaotic cold accretion models, CCA; e.g. King & Pringle 2007; Wada, Papadopoulos & Spaans 2009; Nayakshin, Power & King 2012; Gaspari, Ruszkowski & Oh 2013; Gaspari, Brighenti & Temi 2015; King & Nixon 2015; Gaspari, Temi & Brighenti 2017). Growing observational evidence provide support to this picture, at least for LERGs located in high-density environments (i.e. in rich groups and clusters). The importance of (chaotic) hot gas cooling in more isolated LERGs is still not clear (e.g. Ruffa et al. 2019b, 2022; Maccagni et al. 2023).

In general, both theoretical studies (e.g. Shlosman, Frank & Begelman 1989) and numerical simulations (e.g. Pizzolato & Soker 2005, 2010; Wagner, Bicknell & Umemura 2012; McNamara et al. 2016) have shown that cold gas can play a fundamental role in fuelling nearby AGN (both radiative and kinetic mode), with Ward et al. (2022) finding that AGN are preferentially located in galaxies with high-molecular gas fractions. A corresponding comprehensive observational picture, however, is still missing.

The mm-Wave Interferometric Survey of Dark Object Masses (WISDOM) project is exploiting high-resolution CO observations from the Atacama Large Millimeter/submillimeter Array (ALMA) with the primary aim of measuring SMBH masses in a morphologically diverse sample of nearby galaxies (e.g. Davis et al. 2017; Onishi et al. 2017; Davis et al. 2018; North et al. 2019; Smith et al. 2019; North et al. 2021; Smith et al. 2021a, b; Lelli et al. 2022; Ruffa et al. 2023b). In this paper, we use WISDOM data with a typical spatial resolution of ~ 20 – 30 pc to look for a connection between the circumnuclear molecular gas reservoirs observed with ALMA and the SMBH fuelling across a sample with a wide range of nuclear activities (from low/high-luminosity Seyferts to LERGs). Our main aim is to explore the scenarios described above, testing the cold gas-SMBH fuelling correlations and the scales over which it persists.

This paper is organized as follows. In Section 2, we describe the sample and the multiwavelength observations used for our analysis. We describe the adopted methodology in 3. We present our results in Section 4 and discuss them in Section 5, before summarizing and concluding in Section 6.

2 OBSERVATIONS

2.1 WISDOM sample

WISDOM ALMA data (with a typical resolution of $\approx 0''.1$ or 30 pc) were originally collected with the intent of measuring SMBH masses. The main selection criterion for WISDOM galaxies was thus to have the SMBH sphere of influence (SOI)¹ spatially resolvable with ALMA. Therefore, our sample of galaxies is fairly heterogeneous, containing both nearly quenched ETGs and star-forming spirals with a range of nuclear activities. In particular, here we study data of 35 WISDOM objects, spanning stellar masses M_* from $10^{9.1}$ to

¹The SOI is the region where the gravitational potential of the SMBH dominates over that of the host galaxy and is defined as

$$R_{\text{SOI}} \equiv GM_{\text{BH}}/\sigma_*^2, \quad (1)$$

where M_{BH} is the mass of the SMBH, σ_* is the stellar velocity dispersion of the host bulge and G is the gravitational constant.

Table 1. Physical parameters of the galaxies sample.

Galaxy	Distance (Mpc)	Jet	Galaxy type	AGN type	$\log(M_*/M_\odot)$	Mass Ref	$\log(\text{SFR}/M_\odot \text{ yr}^{-1})$	Project code	Reference
(1)	(2)	(3)	(4)	(5)	(6)	(7)	(8)	(9)	(10)
FRL49	85.7	No	E-S0	Seyfert 2	10.30	L22	0.78	b	Lelli et al. (2022)
FRL1146	136.7	Yes	Sc	Seyfert 1	11.32	M_{K_s}	–	a, b	This work
MRK567	140.6	No	Sc	–	11.26	C17	1.30	a, b	Davis et al. (2022)
NGC0383	66.6	Yes	E-S0	LERG	11.82	MASSIVE	0.00	c, d, e	North et al. (2019)
NGC0404	3.0	No	E-S0	LINER	9.10	S10	–3.04	f	Davis et al. (2020)
NGC0449	66.3	No	SBa	Seyfert 2	10.07	z0MGS	1.19	c, d	Davis et al. (2022)
NGC0524	23.3	No	S0-a	–	11.40	z0MGS	–0.56	e, g, h	Smith et al. (2019)
NGC0612	130.4	Yes	S0-a	LINER	11.76	M_{K_s}	0.85	b, j	Ruffa et al. (2023b)
NGC0708	58.3	Yes	E	LERG	11.75	MASSIVE	–0.29	e, h, i	North et al. (2021)
NGC1194	53.2	No	S0-a	Seyfert 2	10.64	z0MGS	–1.74	j	This work
NGC1387	19.9	No	E-S0	LINER	10.67	z0MGS	–0.68	d, e	Boyce, in preparation
NGC1574	19.3	No	E-S0	–	10.79	z0MGS	–0.91	c, e	Ruffa et al. (2023b)
NGC2110	35.6	No	E-S0	–	10.41	M_{K_s}	–1.41 ²	c, k	This work
NGC3169	18.7	Yes	Sa	Seyfert 1	10.84	z0MGS	0.29	e, i	Davis et al. (2022)
NGC3351	10.0	Yes	Sb	LERG	10.28	z0MGS	–1.29 ²	e, n	This work
NGC3368	18.0	Yes	Sab	LERG	10.67	z0MGS	–0.29	k	Davis et al. (2022)
NGC3607	22.2	No	E-S0	–	11.34	A3D	–0.54	e, i	Davis et al. (2022)
NGC3862	92.5	Yes	E	LERG	11.68	MASSIVE	–0.63 ²	a, e, i, l	This work
NGC4061	94.1	Yes	E	–	11.54	MASSIVE	–0.71	a, e, i, l	Davis et al. (2022)
NGC4261	31.9	Yes	E	LINER	10.80	M_{K_s}	–1.93 ²	a, l	Ruffa et al. (2023b)
NGC4429	16.5	No	S0-a	–	11.17	A3D	–0.84	e, n	Davis et al. (2018)
NGC4435	16.5	No	S0	–	10.69	A3D	–0.84	e, i	Davis et al. (2022)
NGC4438	16.5	No	Sa	LINER	10.75	z0MGS	–0.3	e, i	Davis et al. (2022)
NGC4501	14.0	Yes	Sb	Seyfert 2	11.00	z0MGS	0.43	e, g	Davis et al. (2022)
NGC4697	11.4	No	E	–	11.07	A3D	–1.08	i	Davis et al. (2017)
NGC4826	7.4	No	SABa	Seyfert 1	10.20	z0MGS	–0.71	e, n	Davis et al. (2022)
NGC5064	34.0	No	Sb	–	10.93	z0MGS	0.11	e, g	Davis et al. (2022)
NGC5765b	114.0	No	SABb	Seyfert 2	11.21	M_{K_s}	1.43	j	Davis et al. (2022)
NGC5806	21.4	Yes	Sb	Seyfert 2	10.57	z0MGS	–0.03	d, e	Davis et al. (2022)
NGC5995	107.5	No	SABa	Seyfert 2	11.41	M_{K_s}	–	b	This work
NGC6753	42.0	No	Sb	–	10.78	z0MGS	0.32	e, g	Davis et al. (2022)
NGC6958	30.6	No	E	–	10.76	z0MGS	–0.58	e, g	Thater, in preparation
NGC7052	51.6	Yes	E	LERG ¹	11.75	MASSIVE	–0.07	a, l	Smith et al. (2021a)
NGC7172	33.9	No	Sa	Seyfert 2	10.76	z0MGS	0.38	m	Davis et al. (2022)
PGC043387	95.8	No	E	–	11.12	M_{K_s}	–0.48	i	This work

Notes: (1) Galaxy name, (2) galaxy distance in Mpc, (3) whether a resolved radio jet is present in radio observations of the galaxy, (4) galaxy morphological type, (5) AGN type or HERG/LERG classification (determined using classification from fig. 2 of Best & Heckman 2012). The radio AGN classification of NGC7052 was taken from Gleisinger et al. (2020). (6) Galaxy stellar mass, (7) the reference for the stellar mass: L22 refers to Lelli et al. (2022), C17 refers to Cook et al. (2017), S10 refers to Seth et al. (2010), A3D refers to Cappellari et al. (2013), MASSIVE refers to Veale et al. (2017), and z0MGS to Leroy et al. (2019). M_{K_s} refers to masses estimated from the galaxies K_s -band magnitude using equation (2) of Cappellari (2013). (8) The star formation rate (SFR) of the galaxy. The uncertainties on the SFRs are 0.2 dex for all sources except NGC0404, NGC1194, and PGC043387 which have uncertainties of 0.22, 0.87, and 0.22 dex, respectively. ² represents galaxies where the SFR was estimated in this work. (9) ALMA Project codes of each source, where a: 2016.2.00046.S, b: 2017.1.00904.S, c: 2015.1.00419.S, d: 2016.1.00437.S, e: 2016.2.00053.S, f: 2017.1.00572.S, g: 2015.1.00466.S, h: 2017.1.00391.S, i: 2015.1.00598.S, j: 2016.1.01553.S, k: 2016.1.00839.S, l: 2018.1.00397.S, m: 2019.1.00363.S, and n: 2013.1.00493. (10) Reference where the ALMA data were initially presented.

$10^{11.8} M_\odot$, and 1.4 GHz radio luminosities $L_{1.4\text{GHz}}$ from $\approx 10^{34}$ to $\approx 10^{41}$ ergs s^{-1} . The sample galaxies and their basic parameters are listed in Table 1. The AGN properties of our sample sources are discussed in detail further, and comparisons of these with other literature samples are presented in subsection 4.1.

2.2 ALMA observations and data reduction

Thirty-two sample objects were observed in $^{12}\text{CO}(2-1)$ and 230 GHz continuum using ALMA Band 6, while three (NGC3351, NGC4429, NGC4826) have Band 7 $^{12}\text{CO}(3-2)$ and 345 GHz continuum observations. The ALMA observations used in this work were taken between 2013 and 2020 as part of a large number of projects (see Table 1). For each target we used multiple ALMA observations

with multiple array configurations. This enabled us to reach high-angular resolution, while ensuring adequate UV-plane coverage and excellent flux recovery. The spectral configuration always consisted of four spectral windows (SPWs), one centred on the redshifted frequency of the ^{12}CO line (rest frequency 230.5 GHz for the 2–1 transition, 345.8 GHz for 3–2). The other three SPWs were used to observe the continuum. ALMA data were reduced using the Common Astronomy Software Applications (CASA) pipeline (McMullin et al. 2007) version appropriate for each data set. A standard calibration strategy was adopted for every observation. A single-bright object (typically a quasar) was used as both flux and bandpass calibrator, while a second bright object was used as a phase calibrator. More details on the data-reduction process can be found in Davis et al. (2022).

2.2.1 Line imaging

In this work we make use of the CO data cubes presented in Davis et al. (2022), or used the same cleaning methods described therein for consistency. The final cleaned cubes have synthesized beam sizes ranging from $0''.054$ to $0''.659$, corresponding to spatial scales from 0.8 to 291 pc, and noise levels ranging from 0.19 to 3.70 mJy beam⁻¹. Since we are interested only in the gas reservoirs on scales $\lesssim 100$ pc (i.e. those relevant for the SMBH accretion process), we restrict our analysis to the sub-sample of 29 WISDOM galaxies whose ALMA data cubes satisfy such spatial resolution requirement.

2.3 Ancillary data

We gathered a variety of ancillary data to assess the level of nuclear activity in our targets and test its connection with the cold gas reservoirs observed with ALMA. For each source, we thus retrieved 2–10 keV X-ray, 1.4 GHz radio continuum and optical [O III] λ 5007 luminosities from the NASA Extragalactic Data base (NED)² or other literature sources.

All the ancillary observations used in this work are listed in Appendix Table A1. In the following, we briefly describe each set of ancillary data and caveats around their use.

2.3.1 X-ray data

We retrieved the nuclear 2–10 keV X-ray luminosities ($L_{X, 2-10}$) of the majority of our sources from Bi, Feng & Ho (2020), who presented a catalogue of nearby galaxies observed with *Chandra*. Ten sample galaxies are not included in this catalogue³, thus their X-ray data was gathered from NED and comes from a variety of satellites, that is, Röntgensatellit (*ROSAT*), *Einstein*, Advanced Satellite for Cosmology and Astrophysics (*ASCA*), *XMM-Newton*, and *Chandra* (see Appendix Table A1). For 4 (NGC3351, NGC3862, NGC4429, and NGC4826) out of these 10 galaxies, 2–10 keV luminosities were not available, thus we scaled the available measurement (0.2–2 keV for NGC3351 and NGC4429, 0.3–8 keV for NGC3862 and NGC4826) to the 2–10 keV energy band using a power law with an index -0.8 (corresponding to the mean reported by Reeves & Turner 2000). Eight sample galaxies do not have any X-ray data available.

Thanks to the exquisite *Chandra* resolution ($\approx 0.5''$ on-axis) and the efforts by the authors to remove as much contamination as possible, the nuclear 2–10 keV luminosities from Bi et al. (2020) are expected to trace only emission from the unresolved AGN core (although some negligible contamination from unresolved nuclear X-ray sources may still occur). In the other 10 cases, the spatial resolution of the available X-ray observations does not allow to distinguish between nuclear AGN emission and other types of contribution on larger galaxy scales, thus possible sources of contamination need to be considered. This includes emission from the diffuse hot atmospheres in and around galaxies (i.e. the circumgalactic medium, CGM). This low surface brightness emission, however, usually requires very deep X-ray observations to be detected, and is typically dominant in the softer (0.3–2 keV) energy range. As such, we expect CGM contamination to be minimal even in low resolution 2–10 keV X-ray data. A relatively larger contribution from the CGM may still

be present in faint X-ray sources and in the four cases in which the 2–10 keV luminosities was extrapolated from lower energy bands.

Stellar X-ray binaries are another potential source of contamination. The K-band luminosity has been demonstrated to correlate with the luminosity of low-mass X-ray binaries (LMXB). We thus use the K_s -band flux to estimate the contribution of LMXB to the 2–10 keV emission using the relations from Kim & Fabbiano (2004) and Boroson, Kim & Fabbiano (2011). We find that in 3 of the 10 galaxies for which *Chandra* data was not available from Bi et al. (2020) the contributions from LMXBs is minimal (<5 per cent). In the other seven galaxies (NGC0449, NGC0524, NGC3351, NGC3368, NGC3862, NGC4429, and NGC4826) the contribution expected from up to 43 per cent. To estimate the potential contamination from high-mass X-ray binaries (HMXB) we used the relation between SFR and X-ray luminosity from Grimm, Gilfanov & Sunyaev (2003). In this case, we find three galaxies have minimal contributions (<5 per cent), six (NGC0449, NGC0524, NGC3368, NGC3351, NGC4429, and NGC4826) have larger contributions up to 73 per cent, and one (FRL1146) where we do not have information on the SFRs so we could not calculate the contributions from HMXB. We therefore assume that the 2–10 keV luminosity of most of our targets is dominated by AGN emission from the core. In few individual sources, however, it is possible that we slightly overestimate the AGN luminosity due to the aforementioned uncertainties.

2.3.2 Radio data

We used 1.4 GHz radio observations to probe the type of nuclear activity, and the presence of radio jets in our sources. The data used in this work are mostly from the Very Large Array sky surveys, such as the Faint Images of the Radio Sky at Twenty-Centimeters (FIRST; Becker, White & Helfand 1994), and the NRAO VLA Sky Survey (NVSS; Condon et al. 1998). The spatial resolution of these surveys is typically very poor (e.g. $45''$ for the NVSS). While this does not allow us to resolve nuclear radio structures, it does ensure that no radio emission is resolved out and that any associated large-scale radio jet is detected. For the one source (NGC1574) for which 1.4 GHz observations were not available, we scaled the available 5 GHz radio data to 1.4 GHz using a power law with a spectral index $\alpha = -0.8$ (for $S \propto \nu^\alpha$), as typical for optically thin radio jet emission (e.g. Komissarov & Gubanov 1994; Laing & Bridle 2013).

It is possible that some of the radio emission detected in our targets is contaminated by star formation within the galaxy (e.g. from supernova remnants). To quantify such putative contribution, we gathered the SFRs of our sample sources from Davis et al. (2022), when available, as before. For the six sample galaxies not included in that work, we estimated the SFRs adopting the following relation

$$\text{SFR} = \frac{M_{\text{H}_2}}{\tau}, \quad (2)$$

where M_{H_2} is the total molecular gas mass within the galaxy (calculated as described in subsection 3.1), and τ is the depletion time, assumed to be 2 Gyr (e.g. Leroy et al. 2008). We then estimated the expected 1.4 GHz radio luminosity due to star formation using the following relation (Murphy et al. 2011)

$$\left(\frac{\text{SFR}_\nu}{M_\odot \text{yr}^{-1}} \right) = 10^{-27} \left[2.18 \left(\frac{T_e}{10^4 \text{K}} \right)^{0.45} \left(\frac{\nu}{\text{GHz}} \right)^{-0.1} + 15.1 \left(\frac{\nu}{\text{GHz}} \right)^{\alpha_{\text{NT}}} \right]^{-1} \left(\frac{L_\nu}{\text{erg s}^{-1} \text{Hz}^{-1}} \right), \quad (3)$$

²<https://ned.ipac.caltech.edu/>

³FRL49, FRL1146, NGC0449, NGC0524, NGC1194, NGC3351, NGC3368, NGC3862, NGC4429, and NGC4826.

which can be re-arranged to

$$\left(\frac{L_\nu}{\text{erg s}^{-1}\text{Hz}^{-1}}\right) = 10^{27} \left(\frac{\text{SFR}_\nu}{M_\odot\text{yr}^{-1}}\right) \left[2.18 \left(\frac{T_e}{10^4\text{K}}\right)^{0.45} \left(\frac{\nu}{\text{GHz}}\right)^{-0.1} + 15.1 \left(\frac{\nu}{\text{GHz}}\right)^{\alpha^{\text{NT}}}\right], \quad (4)$$

where ν is the observed frequency, T_e is the electron temperature, and α^{NT} is the non-thermal spectral index. We assumed $T_e = 10^4$ K (Murphy et al. 2011) and $\alpha = -0.8$ (Murphy et al. 2011). The relation combines thermal radio emission (calculated from the ionizing photon production rate) and non-thermal radio emission from supernovae, both of which are related directly to the SFR.

From the ratio between the total radio luminosity and that expected from star formation, $\log_{10}(L_{1.4\text{GHz}}/L_{1.4\text{GHz, SF}})$, we calculate what we call the radio excess factor ($E_{1.4}$). In galaxies with $E_{1.4}$ significantly larger than zero, the detected radio emission cannot be explained by star formation, and thus likely arises from nuclear activity. The radio excess factor for each galaxy is tabulated in Appendix Table A1.

2.3.3 Optical line data

[O III] λ 5007 is typically the strongest emission line in optical spectra of AGN and arises from gas in the narrow-line regions (NLRs) that has been photo-ionized by the AGN radiation. It is then usually considered as a good proxy of the AGN bolometric luminosity (e.g. Heckman & Best 2014). [O III] has also the advantage to be a more ubiquitous tracer of nuclear activity than the 2–10 keV luminosity, as it is observed in both kinetic- and radiative-mode AGN and does not suffer of any obscuration from the dusty torus (present in typical Seyfert-like objects). We therefore collected [O III] λ 5007 luminosities from a variety of instruments/surveys, such as the double spectrograph at the Hale Telescope (Ho, Filippenko & Sargent 1995), El Leoncito Astronomical Complex (CASLEO; Bonatto & Pastoriza 1997; Rodríguez-Ardila, Pastoriza & Donzelli 2000), the DOLORES (Device Optimized for the LOW RESolution) spectrograph at Galileo National Telescope (TNG; Buttiglione et al. 2009), Sloan Digital Sky Survey (SDSS; Zhu et al. 2011), MPG/ESO telescope (Tadhunter et al. 1993), the spectrograph on the Shane Telescope at Lick Observatory (De Robertis & Osterbrock 1986; Crawford et al. 1999), and the CTIO Telescope (Moustakas et al. 2010). We note that the [O III] λ 5007 line may be contaminated by star formation or old stars, or be affected by extinction arising within the host galaxy. However, star formation is only expected to contribute significantly in higher redshift galaxies (whereas it should be negligible in nearby objects such as our sample sources; Suzuki et al. 2016). Where available, we additionally gathered H β , [N II] λ 6583, and H α luminosities. These are useful to calculate the [O III]/H β and [N II]/H α ratios which we can use to construct the BPT diagrams of our objects, and thus assess their dominant excitation mechanism (e.g. Baldwin, Phillips & Terlevich 1981; Kewley et al. 2006). Eighteen of our sample galaxies have all the lines required to construct a BPT diagram, showing that 5 sources fall in the AGN-dominated region (FRL49, NGC0612, NGC1194, NGC2110, NGC5765b), 4 in the LINER region (NGC3368, NGC3862, NGC5995, NGC6753), 8 in the composite region (NGC1387, NGC3351, NGC4061, NGC4261, NGC4826, NGC5064, NGC7172, PGC043387), and 1 (MRK567) in the SF-dominated region. The $\log([O III]/H\beta)$ ratios for 9 other galaxies (FRL1146, NGC0404, NGC0524, NGC3169, NGC3607, NGC4429, NGC4435, NGC4438, NGC4501) have values ranging from -0.44 to 0.71 . Depending on their unknown $\log([N II]/H\alpha)$

ratios, they could thus be placed in the star formation, composite, LINER regions or AGN regions.

2.3.4 ALMA nuclear continuum emission

We gathered the ALMA nuclear continuum luminosities from Ruffa et al. (2023a), with the mm-continuum flux which have been measured from the innermost beam at the position of the AGN in the ALMA continuum map of each galaxy.

2.3.5 Accretion tracer correlations

The correlations between the nuclear mm luminosity, X-ray luminosity, [O III] luminosity and excess radio factor are shown in Fig. 1, with the correlation coefficients and p-values listed in Table 3. This figure shows that the four tracers of activity mostly correlate with each other despite different contaminants, suggesting we are tracing nuclear activity rather than larger-scale emission. This also shows that, even though some of the galaxies in our sample are not formally classified as AGN, low level nuclear activity seems to be present.

2.3.6 Stellar masses

The stellar masses of the majority of our sample galaxies were taken from Davis et al. (2022), who in turn collected them from the ATLAS^{3D} (Cappellari et al. 2013) and MASSIVE (Veale et al. 2017) surveys, and the $z = 0$ Multiwavelength Galaxy Synthesis (z0MGS) project (Leroy et al. 2019). The stellar masses for MRK 567 and NGC 0404 were taken from Cook et al. (2017) and Seth et al. (2010), respectively. Where stellar-mass measurements were not available in the literature, we estimated them from the K_s -band magnitudes measured in the extended source catalogue of the 2 micron All-Sky Survey (2MASS; Jarrett et al. 2003). We used equation 2 of Cappellari (2013), with no correction for the emission from the AGN (as this should be small at these frequencies in our low luminosity sources)

$$\log_{10}M_* \approx 10.58 - 0.44 \times (M_{K_s} + 23), \quad (5)$$

where M_* is the stellar mass and M_{K_s} is the K_s -band magnitude.

3 METHODOLOGY AND DERIVED QUANTITIES

In this work, we search for correlations between circumnuclear molecular gas reservoirs and SMBH fuelling across a sample of galaxies with a range of nuclear activities. This requires us to assess both the amount of molecular gas present in the circumnuclear regions, and its structure. Furthermore, we need to constrain the SMBH accretion rate in our sources, and the type of nuclear activity. Further we describe the methodology we adopted to determine these quantities.

3.1 Molecular gas masses

We adopt the following relation to estimate the molecular hydrogen gas masses (M_{H_2}) of our galaxies within different apertures (Bolatto, Wolfire & Leroy 2013):

$$M_{\text{H}_2} = 2m_{\text{H}} \frac{\lambda^2}{2k_{\text{B}}} X_{\text{CO}} D_{\text{L}}^2 R \int S_\nu d\nu, \quad (6)$$

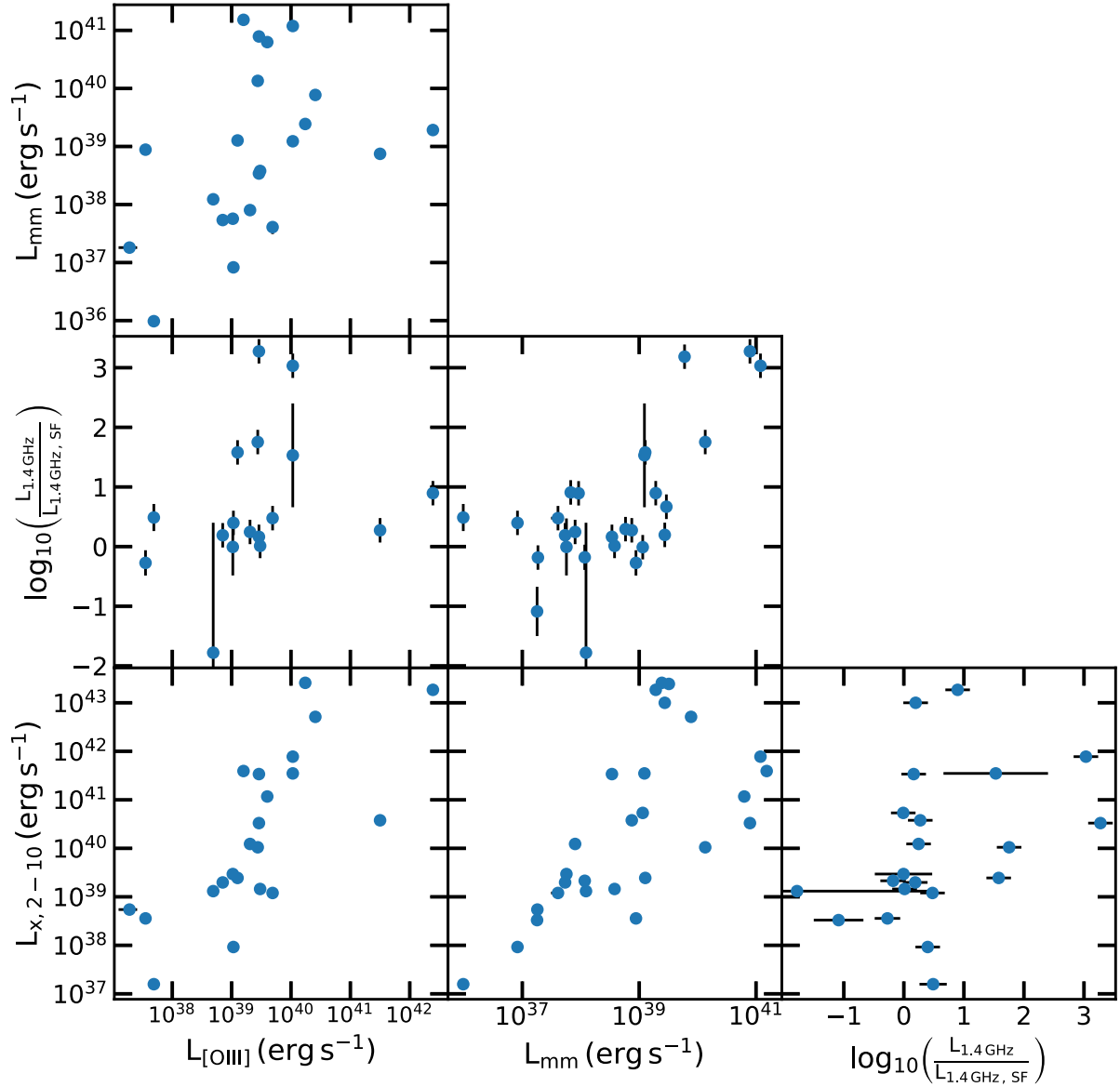


Figure 1. Correlations between the nuclear mm continuum luminosity, excess 1.4 GHz factor, 2–10 keV luminosity and the [O III] luminosity. The Spearman rank coefficients and p -value of these correlations are listed in Table 3.

where m_{H} is the mass of the hydrogen atom, λ is the rest wavelength of the observed molecular transition, k_{B} is the Boltzmann constant, X_{CO} is the CO-to- H_2 conversion factor, D_{L} is the luminosity distance, $R \equiv T_{\text{b, ref}}/T_{\text{b, CO(1-0)}}$ is the line intensity ratio (i.e. the ratio between the ground state and the observed CO line brightness temperature), and $\int S_{\nu} dV$ is the integrated flux density of the CO(1-0) line, with units matching those of X_{CO} . This was estimated by integrating the spectrum of the observed CO transition within a given aperture over all the velocity channels of the line. Equation (6) can be simplified to

$$\left(\frac{M_{\text{H}_2}}{M_{\odot}}\right) = 7847 J_{\text{upper}}^{-2} X_{\text{CO}, 2 \times 10^{20}} R \left(\frac{D_{\text{L}}}{\text{Mpc}}\right)^2 \left(\frac{\int S_{\nu} dV}{\text{Jy km s}^{-1}}\right), \quad (7)$$

where J_{upper} is the upper state rotational quantum number of the observed transition (here J_{upper} is 2 or 3) and $X_{\text{CO}, 2 \times 10^{20}} = \frac{X_{\text{CO}}}{2 \times 10^{20} \text{ cm}^{-2} (\text{K km s}^{-1})^{-1}}$. As most of our galaxies are massive and metal rich, we assume a Milky Way like CO-to- H_2

conversion factor of $3 \times 10^{20} \text{ cm}^{-2} (\text{K km s}^{-1})^{-1}$ (Strong et al. 1988). We also assume the line ratios to be $T_{\text{b, CO(2-1)}/T_{\text{b, CO(1-0)}} = 0.7$ and $T_{\text{b, CO(3-2)}/T_{\text{b, CO(1-0)}} = 0.3$ (see e.g. Leroy et al. 2022). For sample galaxies observed with ALMA at adequate spatial resolutions, we estimated the molecular gas mass within three different elliptical apertures of radii 100, 75, and 50 pc. We additionally measure the molecular gas mass in a elliptical aperture with a radius of 200 pc to measure the nuclear molecular gas concentration. The resulting M_{H_2} are listed in Table 2. As mentioned earlier, the molecular gas masses were all calculated with a fixed X_{CO} factor. We note, however, that the CO-to- H_2 conversion factors in galaxy centres may vary (Sandstrom et al. 2013), adding uncertainty at a ~ 0.3 dex level. To aid comparisons with different X_{CO} prescriptions, we provide the CO integrated flux densities measured within the different apertures in Appendix Table A3. We assume an additional 10 per cent error on our molecular gas masses due to ALMA calibration uncertainties.

Table 2. Circumnuclear masses for different region sizes and millimetre spectral indices for our sources.

Galaxy	$\log \left(\frac{M_{\text{H}_2}}{M_\odot} \right)$ (200 pc)	$\Delta \log M_{\text{H}_2}$ (dex)	$\log \left(\frac{M_{\text{H}_2}}{M_\odot} \right)$ (100 pc)	$\Delta \log M_{\text{H}_2}$ (dex)	$\log \left(\frac{M_{\text{H}_2}}{M_\odot} \right)$ (75 pc)	$\Delta \log M_{\text{H}_2}$ (dex)	$\log \left(\frac{M_{\text{H}_2}}{M_\odot} \right)$ (50 pc)	$\Delta \log M_{\text{H}_2}$ (dex)	$S_{\nu, \text{mm}}$ (mJy)	$\sigma S_{\nu, \text{mm}}$ (mJy)
(1)	(2)	(3)	(4)	(5)	(6)	(7)	(8)	(9)	(10)	(11)
FRL49	8.34	0.04	7.87	0.04	–	–	–	–	0.93	0.038
FRL1146	–	–	–	–	–	–	–	–	0.47	0.0272
MRK567	8.90	0.04	8.52	0.04	–	–	–	–	<0.11	0.0354
NGC0383	8.15	0.04	7.71	0.04	7.48	0.04	7.08	0.04	63	0.101
NGC0404	6.18	0.04	6.18	0.04	6.17	0.04	6.14	0.04	0.38	0.012
NGC0449	–	–	–	–	–	–	–	–	0.60	0.0246
NGC0524	7.42	0.04	6.93	0.05	6.75	0.04	6.47	0.04	5.7	0.023
NGC0612	8.20	0.04	7.62	0.04	7.50	0.04	7.35	0.05	25	0.06
NGC0708	8.12	0.04	7.66	0.04	7.47	0.04	7.13	0.05	1.3	0.0165
NGC1194	7.48	0.04	7.13	0.04	6.95	0.05	–	–	1.6	0.0286
NGC1387	7.66	0.04	7.05	0.04	6.80	0.04	6.43	0.04	1.0	0.0535
NGC1574	6.79	0.04	6.74	0.04	6.66	0.04	6.40	0.04	3.3	0.033
NGC2110	7.35	0.04	6.77	0.04	–	–	–	–	21	0.453
NGC3169	8.26	0.04	7.80	0.04	7.60	0.04	–	–	3.4	0.107
NGC3351	7.66	0.04	7.39	0.04	7.16	0.04	6.91	0.04	<0.45	0.148
NGC3368	8.36	0.04	7.87	0.04	7.68	0.05	7.42	0.04	<0.56	0.202
NGC3607	7.89	0.04	7.51	0.04	7.33	0.04	–	–	2.7	0.164
NGC3862	–	–	–	–	–	–	–	–	64	1.43
NGC4061	7.65	0.04	7.10	0.04	6.90	0.04	–	–	2.4	0.18
NGC4261	7.32	0.04	7.29	0.04	7.21	0.04	7.02	0.04	220	1.53
NGC4429	7.31	0.04	6.64	0.04	6.38	0.04	5.88	0.04	1.1	0.0853
NGC4435	7.61	0.04	7.25	0.04	7.05	0.05	6.78	0.04	0.73	0.0246
NGC4438	8.19	0.04	7.78	0.04	7.58	0.04	7.24	0.04	0.52	0.126
NGC4501	8.06	0.04	7.72	0.04	7.52	0.05	7.22	0.04	1.4	0.0789
NGC4697	6.02	0.04	5.93	0.04	5.83	0.04	5.61	0.04	0.48	0.0444
NGC4826	7.66	0.04	7.55	0.04	7.25	0.04	7.60	0.04	0.38	0.0746
NGC5064	8.13	0.04	7.67	0.04	7.41	0.04	7.10	0.04	0.28	0.0259
NGC5765b	8.41	0.04	–	–	–	–	–	–	0.328	0.0616
NGC5806	7.57	0.04	7.16	0.04	7.02	0.04	6.77	0.05	<0.14	0.0473
NGC5995	–	–	–	–	–	–	–	–	0.99	0.0331
NGC6753	8.63	0.04	8.16	0.05	7.94	0.04	7.62	0.04	<0.14	0.0447
NGC6958	7.70	0.04	7.17	0.04	6.96	0.04	6.61	0.04	11	0.0569
NGC7052	7.75	0.04	7.39	0.04	7.17	0.04	6.79	0.04	18	0.0823
NGC7172	8.36	0.04	7.48	0.04	7.14	0.04	6.74	0.04	8.4	0.32
PGC043387	–	–	–	–	–	–	–	–	<0.31	0.104

Notes: (1) Galaxy name. (2) Mass measured within a elliptical aperture of 200 pc radius, with its uncertainty in (3). (4)–(9) Follow the same pattern, for 100, 75, and 50 pc apertures. (10) Nuclear mm continuum flux derived from all our ALMA data (fluxes measured separately from the lower and upper sidebands in Appendix Table A), (11) Nuclear mm continuum flux uncertainty.

To assess the structure of the molecular gas at the centre of each sample galaxy, following García-Burillo et al. (2021), we also calculated the molecular concentration parameter

$$\frac{\Sigma_{\text{H}_2}^{50\text{pc}}}{\Sigma_{\text{H}_2}^{200\text{pc}}} = 16 \left(\frac{M_{\text{H}_2}^{50\text{pc}}}{M_{\text{H}_2}^{200\text{pc}}} \right), \quad (8)$$

where $\Sigma_{\text{H}_2}^{x\text{pc}}$ and $M_{\text{H}_2}^{x\text{pc}}$ are the molecular gas surface-density and mass, respectively, within a elliptical aperture of radius x pc. We assumed that the gas lies within a flat disc so $\Sigma_{\text{H}_2}^{x\text{pc}} = \frac{M_{\text{H}_2}^{x\text{pc}}}{\pi x^2}$.

3.2 Accretion rates

To estimate the SMBH accretion rates in each source, we use the following relation (Alexander & Hickox 2012)

$$\left(\frac{\dot{M}_{\text{BH}}}{M_\odot \text{yr}^{-1}} \right) = 0.15 \left(\frac{0.1}{\eta} \right) \left(\frac{L_{\text{Bol}}}{10^{45} \text{ ergs s}^{-1}} \right), \quad (9)$$

where L_{Bol} is the AGN bolometric luminosity and η is the mass–energy conversion efficiency factor, typically assumed to be 0.1 (e.g. Marconi et al. 2004).

We follow two prescriptions to estimate the AGN bolometric luminosities. The 2–10 keV X-ray luminosity is generally considered a good proxy of the AGN bolometric luminosity in radiative-mode AGN (e.g. Ho 2008), as X-ray emission in these sources is expected to come from the corona above the accretion disc. In this case, the bolometric luminosity can be calculated by inverting the bolometric correction relation of Marconi et al. (2004):

$$\log_{10} \left(\frac{L_{\text{Bol}}}{L_{2-10\text{keV}}} \right) = 1.54 + 0.24\mathcal{L} + 0.012\mathcal{L}^2 - 0.0015\mathcal{L}^3, \quad (10)$$

where $\mathcal{L} \equiv \log_{10} \left(\frac{L_{\text{Bol}}}{L_\odot} \right) - 12$.

In kinetic-mode AGN, the accretion disc is expected to be absent and the 2–10 keV emission may instead arise from inverse-Compton upscattering of non-thermal photons from the radio jet (e.g. Blundell et al. 2006). For this reason, we additionally used the [O III] λ 5007 luminosity as a proxy of L_{Bol} , adopting the bolometric correction

$L_{\text{bol}}/L_{[\text{OIII}]\lambda 5007} \approx 3500$ (Heckman et al. 2004), to ensure both types of AGN are covered. $[\text{O III}]\lambda 5007$ is a more ubiquitous tracer of nuclear activity as it is usually the brightest emission-line in optical spectra of AGN and is less contaminated than other emission lines. As illustrated in Table 1, a clear AGN classification is missing for some of our sample galaxies (13/35), whereas the majority of them consist on a mix of radiative- and kinetic-mode AGN. For each source, we thus calculate L_{bol} using both the 2–10 keV and $[\text{O III}]\lambda 5007$ luminosity as tracers. We show the relation between these two derived bolometric luminosities in Appendix Fig. A1. We note there is reasonably large scatter in the two measures of bolometric luminosity. This is likely due to the mix of radiative- and kinetic-mode objects in our sample, with the X-ray emission not being a good proxy for the bolometric luminosity of the latter (see earlier). The accretion rates and associated errors for both prescriptions are presented in Table A2.

4 RESULTS AND ANALYSIS

4.1 Properties of WISDOM AGN

As discussed earlier, in this work we aim to investigate previous claims that at circumnuclear scales (<100 pc) accretion rate tracers correlate with the mass and structure of the cold molecular gas mass. As illustrated in Table 1, our sample consists on systems with a diverse range of nuclear activities. In order to further place the WISDOM galaxies in context with previous studies, in Fig. 2 we illustrate the main properties of the AGN in our sample (i.e. bolometric luminosity, black hole mass, Eddington ratio⁴, central velocity dispersion, and jet power), compared with those from the works of Izumi et al. (2016), Babyk et al. (2019), and García-Burillo et al. (2021), with the medians for the samples used and the KS test p -values between the sample are shown in Appendix Table A4. In this work we calculated the jet power using the same method as Babyk et al. (2019). We calculated the radio power using the relation

$$P_{\nu_0} = 4\pi D_L^2 (1+z)^{\alpha-1} S_{\nu_0} \nu_0. \quad (11)$$

This was then used to calculate the jet power using this relation from Cavagnolo et al. (2010)

$$\log P_{\text{cav}} = 0.75 \log P_{1.4} + 1.91. \quad (12)$$

It is clear from Fig. 2 that the bolometric luminosities of our AGN are consistent with those of the samples studied by Izumi et al. (2016) and García-Burillo et al. (2021), and we probe a range of radio jet powers similar to that of the sources analysed by Babyk et al. (2019). Alternatively, the SMBH masses of the AGN in our sample are larger – on average – than those probed in such previous studies, and thus their Eddington ratios are slightly lower (at least when compared with the work of Izumi et al. 2016).

More generally, Fig. 2 shows that there is overlap between the main properties of the AGN in our sample and those in the previous reference studies, with the WISDOM objects being also clearly complementary to such works. In the following subsection, we will further discuss potential differences and if/how these may affect our results.

⁴The Eddington ratio is a measure of the level of nuclear activity and is defined as $\lambda_{\text{Edd}} = L_{\text{bol}}/L_{\text{Edd}}$, where L_{bol} is the AGN bolometric luminosity and $L_{\text{Edd}} = 1.26 \times 10^{38} M_{\text{BH}} \text{ erg s}^{-1}$ is the Eddington luminosity.

4.2 AGN luminosity–molecular gas mass correlations

In Figs 3–5 we show the obtained circumnuclear H_2 masses plotted against excess 1.4 GHz continuum, 2–10 keV X-ray and nuclear mm-continuum luminosity, respectively. To check for the statistical significance of such relations, we carried out a Spearman rank analysis, where we consider relations with p -values ≤ 0.05 as statistically significant. The resulting Spearman rank coefficients and p -values are presented in Table 3

4.2.1 Excess radio luminosity–molecular mass correlation

We show in Fig. 3 the correlation between molecular gas mass on sub-kiloparsec scales and excess radio emission. There is no strong correlation between these quantities, as indicated by Spearman rank analysis (reported in the first row of Table 3). The correlation coefficient is 0.32 for the 100 pc radius aperture, and increases to 0.35 for the 75 pc and 0.56 for the 50 pc radius aperture, with p -values of 0.12, 0.11, and 0.01, respectively. We note that, based on these results, a mild correlation may be present at the 50 pc scale. However, we checked that this is driven by galaxies that are dominated by star formation. When these objects are excluded, the Spearman rank coefficient becomes -0.07 , with a p -value of 0.82, thus finding no evidence for any correlation.

4.2.2 X-ray luminosity–molecular gas mass correlation

We show in Fig. 4 the relation between the molecular gas mass on sub-kiloparsec scales and 2–10 keV X-ray luminosity. Also in this case, there is no significant correlation between the two quantities within any aperture size, as supported by the Spearman rank analysis (reported in the second row of Table 3). The correlation coefficients are 0.31 with a p -value of 0.16 for the case of the molecular gas mass calculated within a 100 pc radius aperture, 0.29 with a p -value of 0.21 for the 75 pc radius aperture, and 0.29 with a p -value of 0.26 for the 50 pc radius aperture.

4.2.3 mm continuum luminosity–molecular gas mass correlation

The nuclear millimetre continuum luminosity is another proxy of the nuclear activity. Indeed, excess mm luminosity has been observed in AGN-hosting galaxies, with the excess being attributed to the AGN itself (e.g. Behar et al. 2015; Doi & Inoue 2016; Behar et al. 2018; Wu, Feng & Fan 2018; Kawamuro et al. 2022). We show in Fig. 5 the total nuclear millimetre luminosity (calculated on scales $\lesssim 200$ pc) against the molecular gas mass on sub-kiloparsec scales, again finding no correlation between the two. The lack of correlation is supported by the Spearman rank analysis (reported in the third row of Table 3). The correlation coefficients are 0.002, 0.14 and 0.11 with p -values 0.99, 0.55, and 0.66 for the 100, 75, and 50 pc regions, respectively.

4.3 Accretion rate–mass correlation

In Figs 6 and 7 we investigate relations between the molecular gas mass and AGN accretion rate, as calculated using the 2–10 keV and $[\text{O III}]$ line luminosity proxies. Also in this case, we do not find any clear correlation. The corresponding Spearman rank analysis (reported in the fourth and fifth rows of Table 3) mostly confirms this scenario.

For accretion rates calculated using the 2–10 keV luminosity as a proxy, a Spearman rank correlation coefficient of 0.31 with

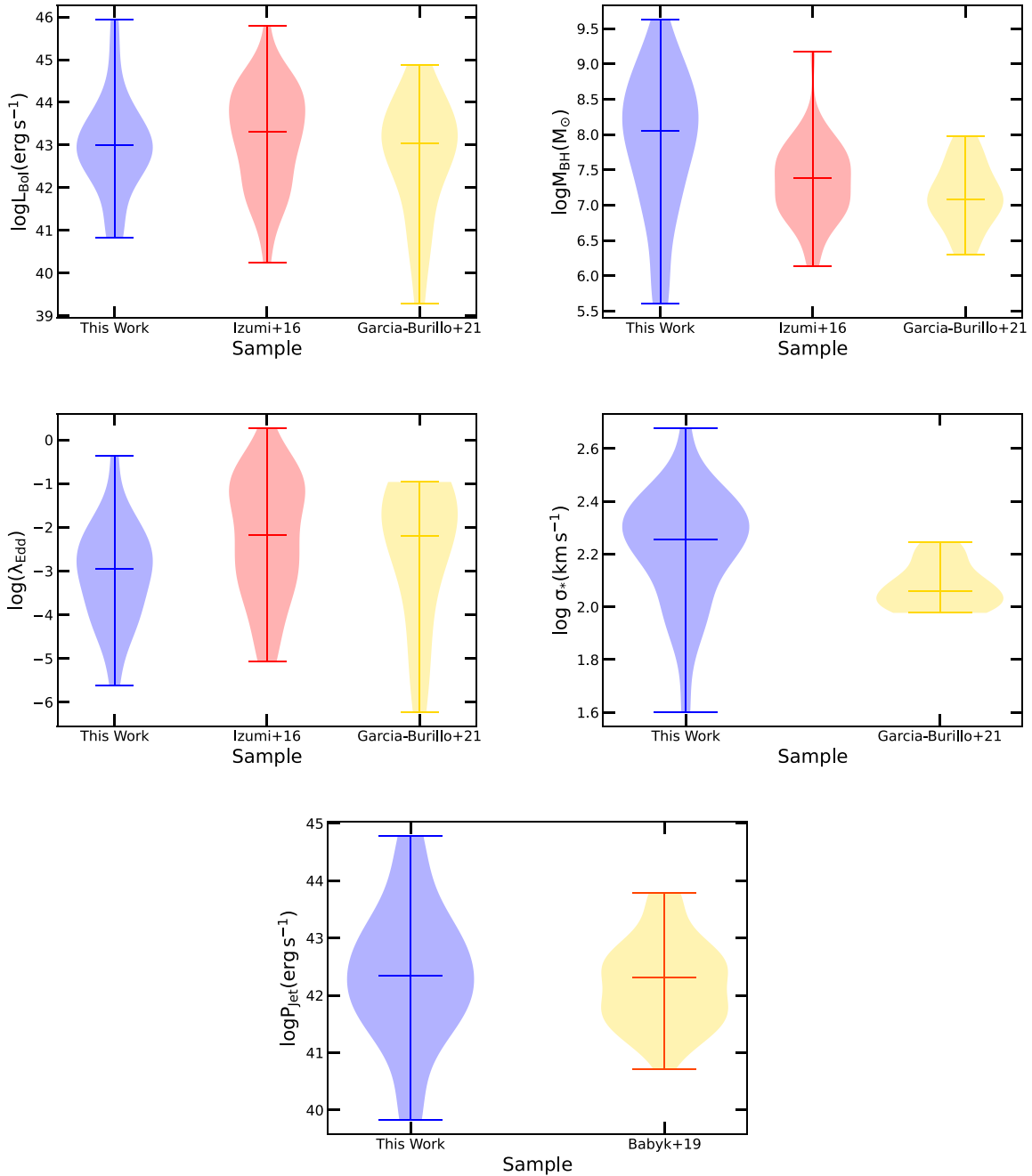


Figure 2. Distribution of AGN bolometric luminosity (top left), black hole mass M_{BH} (top right), Eddington ratio λ_{Edd} (middle left), velocity dispersion (middle right), and jet power (bottom) of the WISDOM sample. These are compared with the properties of the AGN from the works of Izumi et al. (2016), Babyk et al. (2019), and García-Burillo et al. (2021) which are discussed further in the text. The horizontal lines represent the median of each distribution.

a p -value of 0.16 is obtained for the 100 pc radius aperture. For the 75 and 50 pc regions, the Spearman rank coefficients are 0.29 and 0.29, respectively, with associated p -values of 0.21 and 0.26.

For accretion rates calculated using the [O III] line luminosity as a proxy, the Spearman rank coefficients are 0.27, 0.38, and 0.53 with p -values of 0.26, 0.13, and 0.05 for the 100, 75, and 50 pc regions, respectively. These values imply that – as the aperture size decreases – a mildly significant correlation seems to be present. Whether this is real or coincidental due to the reduced number of data points should be investigated further.

5 DISCUSSION

5.1 AGN activity and the circumnuclear molecular gas

As described earlier, we do not find any strong correlation between the masses of molecular gas in the nuclear regions of our diverse sample galaxies and their AGN activities, as traced in a variety of ways. This is despite multiple authors reporting such correlations when studying specific AGN-selected samples of galaxies (e.g. Izumi et al. 2016; Babyk et al. 2019; Koss et al. 2021). Our galaxies were not selected to be AGN, but do cover similar ranges of AGN properties (see Fig. 2).

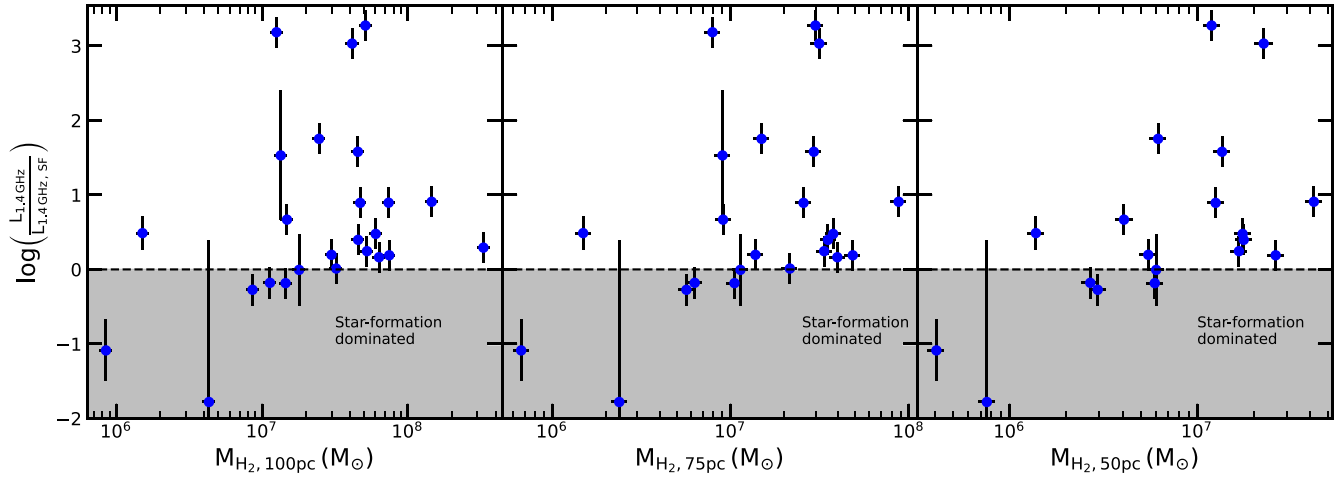


Figure 3. Molecular gas mass within an aperture of a given radius (100, 75, and 50 pc, as indicated by the x-axis labels) versus excess 1.4 GHz radio continuum fraction (after the contribution from star formation has been removed).

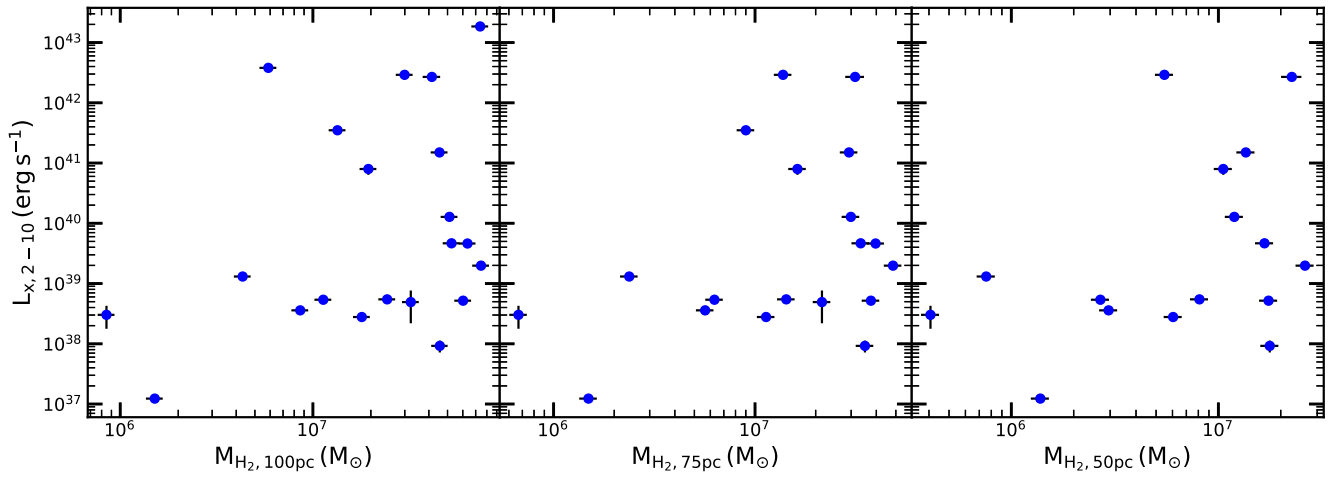


Figure 4. As Fig. 3, but for the 2–10 keV X-ray luminosity.

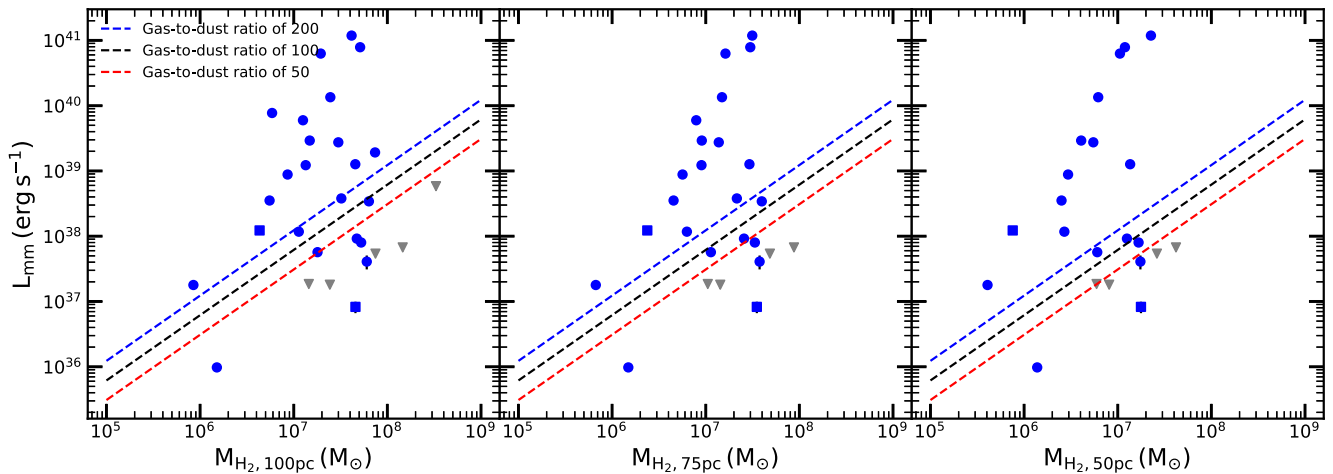


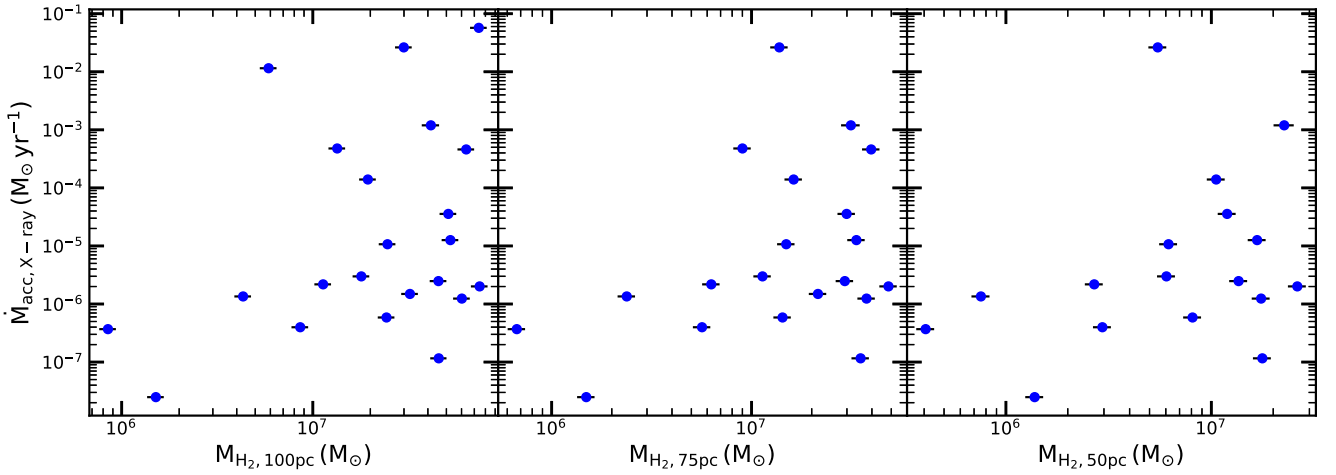
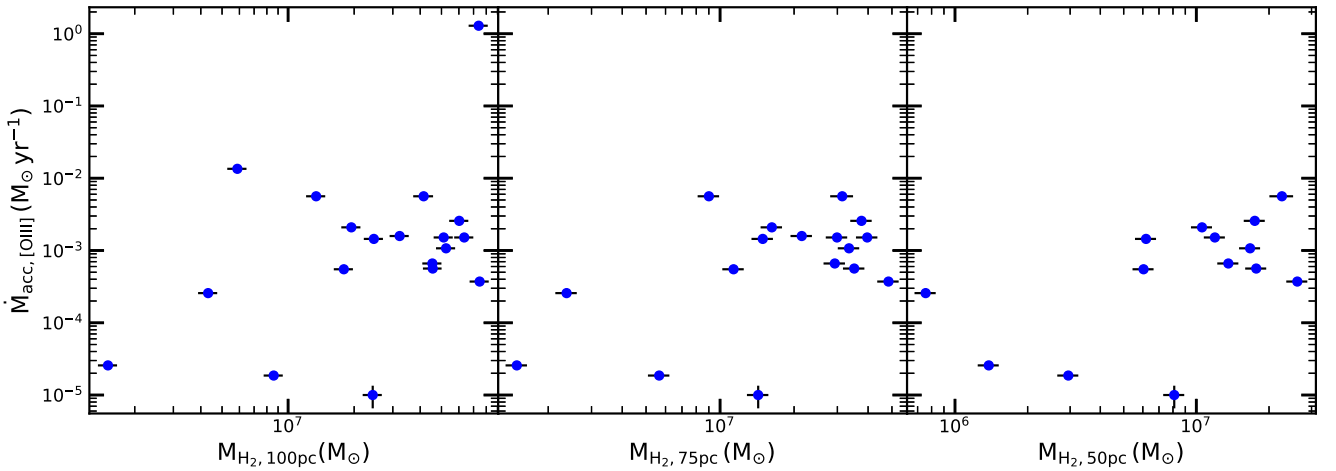
Figure 5. As Fig. 3, but for the nuclear mm-continuum luminosity. Grey triangles are used for the upper limits (calculated as three times the rms noise level) of galaxies undetected in the mm continuum.

Table 3. Spearman rank coefficients and p -values.

Mass–luminosity correlations						
	$\log(M_{\text{H}_2, 100\text{pc}}/M_\odot)$		$\log(M_{\text{H}_2, 75\text{pc}}/M_\odot)$		$\log(M_{\text{H}_2, 50\text{pc}}/M_\odot)$	
	(1)		(2)		(3)	
	Coefficient	p -value	Coefficient	p -value	Coefficient	p -value
$\log(E_{1.4})$	0.32	0.12	0.35	0.11	0.56	0.01
$\log(L_{X, 2-10})$	0.31	0.16	0.29	0.21	0.29	0.26
$\log(L_{\text{mm}})$	0.002	0.99	0.14	0.55	0.11	0.66
$\log(\dot{M}_{\text{acc}, X\text{-ray}})$	0.31	0.16	0.29	0.21	0.29	0.26
$\log(\dot{M}_{\text{acc}, [\text{OIII}]})$	0.27	0.26	0.38	0.13	0.53	0.05

Luminosity–luminosity correlations		
	Coefficient	p -value
	(4)	
$L_{\text{mm}} - L_{X, 2-10}$	0.76	3.37E-6
$L_{\text{mm}} - E_{1.4}$	0.57	0.008
$E_{1.4} - L_{X, 2-10}$	0.16	0.56
$L_{[\text{OIII}]} - L_{X, 2-10}$	0.78	2.27E-5
$L_{[\text{OIII}]} - E_{1.4}$	0.15	0.60
$L_{[\text{OIII}]} - L_{\text{mm}}$	0.52	0.01

Notes: (1) Spearman rank correlation coefficients and p -value for the 100 pc radius aperture, (2) and (3) same quantities for the 75 and 50 pc radius apertures. (4) Lists the Spearman rank correlation coefficients and p -values between the luminosities studied.


Figure 6. As Fig. 3, but for the X-ray-traced accretion rate.

Figure 7. As Fig. 3, but for the [OIII]-traced accretion rate.

Our results suggests that the level of nuclear activity in a given galaxy cannot purely depend on the amount of cold gas around its SMBH. This supports recent work by Molina et al. (2023), where no correlation between the CO(2-1) and AGN luminosity has been reported. In this work, Molina et al. (2023) looked at the correlations between the cold molecular gas mass and AGN properties in a sample of radiative-mode AGN at $z \lesssim 0.5$, using the 5100 Å AGN luminosity as analogy for the AGN bolometric luminosity. In this way, they initially find a weak correlation between CO(2-1) and AGN luminosity, but this then disappears when correcting for the cosmic evolution of the molecular gas content in galaxies. This also clearly highlights that the mechanism(s) driving gas from the wider galaxy scales to the nuclear regions are likely to be different in different types of AGN, and that time-scale variations may be important. Further we discuss each of our tracers, and the conclusions that can be drawn from the differences between our results and others in literature.

5.1.1 X-ray emission

As described in subsections 4.2.2 and 4.3 (and illustrated in Figs 4 and 6, respectively), there is no correlation between the cold molecular gas masses in the circumnuclear regions and the X-ray luminosities/X-ray derived accretion rates of our sample galaxies. These results are consistent with those found in other recent works. Rosario et al. (2018) looked at the relationship between the 2–10 keV X-ray luminosity and the CO(2-1) brightness in a sample of Seyfert galaxies with X-ray luminosities that fall within the range of those studied in our work ($\approx 10^{41.5} - \approx 10^{43.5} \text{ erg s}^{-1}$). The authors find no correlation between the two quantities, and ascribe that to the differences between the spatial scale probed by the single-dish beam and that of the SMBH accretion disc. García-Burillo et al. (2021) also studied the correlation between the molecular gas mass on kpc scales (0.4–1.2 kpc) and the X-ray luminosity in a sample of nearby Seyferts with similar $L_{X, 2-10}$ ($\approx 10^{39} - \approx 10^{44} \text{ erg s}^{-1}$) and molecular gas masses ($\approx 10^{6.5} - \approx 10^{9.5} M_{\odot}$) to the objects studied in this work, finding again no correlation between the two quantities. In this case, the lack of correlation is explained by the different spatial scales and time-scales involved with the last steps of the SMBH fuelling process and the kiloparsec-scales molecular gas reservoirs.

These results are in contrast to Izumi et al. (2016), who reported a positive correlation between the dense ($n_{\text{H}_2} \gtrsim 10^{4-5} \text{ cm}^{-3}$) molecular gas mass at $\approx 100 \text{ pc}$ scales and the X-ray traced accretion rates (calculated using the same methods adopted here) onto the SMBHs of a small sample of 10 nearby Seyfert galaxies. This was interpreted as supporting the role of CNDs in the AGN fuelling process.

Differences between their results and ours may arise for several reasons. First, as also discussed in Rosario et al. (2018) and García-Burillo et al. (2021) it is believed that in radiative-mode AGN X-ray emission traces recently accreted material, as in these cases X-rays are expected to be produced very close to the central SMBH (e.g. Galeev, Rosner & Vaiana 1979). In this scenario, X-ray emission can be highly time variable. However, it would take dynamical time-scales of several hundred thousand years for the gas at the scales we are investigating to fall onto the SMBHs. This difference in time-scales and spatial scales could explain why we do not find correlation between the circumnuclear gas mass and the X-ray luminosity.

Izumi et al. (2016) also investigated the correlation between dense molecular gas mass of the CND and accretion rate only in ten Seyfert galaxies, whereas we consider a >3 times larger sample of galaxies with a varied range of nuclear activities (see Fig. 2) and AGN types

(see Table 1). However, even when considering only the Seyferts in our sample, our results remain unchanged.

Furthermore, the correlation reported by Izumi et al. (2016) involves the dense ($n_{\text{H}_2} \gtrsim 10^{4-5} \text{ cm}^{-3}$) molecular gas mass of the CNDs, estimated using the HCN molecule as tracer. Here we instead use the total molecular gas mass on circumnuclear scales, which has been estimated via CO emission. However, we still cannot make the Seyfert galaxies in our sample follow the correlation of Izumi et al. (2016) without requiring extremely low dense-gas fractions that also vary wildly between galaxies, a behaviour currently not observed in these kind of objects (e.g. Jiménez-Donaire et al. 2019).

We also note that the lack of correlation may be also ascribed to contamination from other (unresolved) sources of X-ray luminosity in the galaxies, such as stellar X-ray binaries (see subsection 2.3.1). However, even when restricting our analysis only to sources observed at high-spatial resolution with *Chandra* (i.e. where the nuclear emission from the AGN can be spatially isolated), we still do not observe any correlation. This suggests that contamination is not driving our results.

Another more speculative possibility that could explain the lack of correlation is that different mechanisms usually give rise to the observed X-ray emission in different AGN types. In radiative-mode AGN such as Seyferts, X-rays are typically produced by inverse-Compton upscattering of photons from the accretion disc by the corona (Ciotti & Ostriker 1997). Whilst, in kinetic-mode AGN, classic accretion discs are either not present or truncated at inner radii (see Section 1), and X-ray emission likely arises from other processes, such as Compton upscattering of non-thermal photons from the radio jets (e.g. Blundell et al. 2006). These two emission processes may not correlate directly or may differ in how they correlate with the cold molecular gas mass of the circumnuclear regions.

Finally another more speculative possibility is that the Seyfert galaxies observed by Izumi et al. (2016) may have been caught in a special phase with bright HCN emission, possibly suggesting a bias in the sample selection. Such bright HCN emission may be more common in Seyferts with sizeable dense molecular gas reservoirs, leading also to higher accretion rates than most of those probed by our sample. Further investigation of diverse galaxy samples in central regions $<50 \text{ pc}$ in radius and using denser gas tracers will allow us to confirm/discard this hypothesis.

5.1.2 Radio emission

Babyk et al. (2019) reported a correlation between the molecular gas mass up to kpc scales and jet power in a sample of nearby ETGs, most of which are LERGs. We wanted to expand this study probing the gas mass down to circumnuclear scales and in a more diverse sample of galaxies. If the results reported by Babyk et al. (2019) held at circumnuclear scales, we would have expected to observe at least some correlation between the circumnuclear gas masses of our sample galaxies and the excess 1.4 GHz radio luminosities (as $P_{\text{jet}} \propto L_{1.4}$; e.g. Cavagnolo et al. 2010). As discussed in subsection 4.2.1 and illustrated in Fig. 3, we do not find any sign of such correlation in this work. This could be explained if the correlation reported by Babyk et al. (2019) does not have anything to do with the SMBH fuelling, but instead arise because more massive galaxies tend to have more massive SMBHs, thus producing higher-power radio jets (Liu, Jiang & Gu 2006). Babyk et al. (2019) also report a link between the hot X-ray-emitting diffuse gas and the molecular gas content in their sample galaxies. This correlation is

explained by the cooling of hot gas which is turned into molecular gas in the galaxy. This cooling of hot gas may then be connected to the radio power in these galaxies and would explain why we do not find a correlation at circumnuclear scales. We note that a result similar to that of Babyk et al. (2019) has been recently reported by Fujita et al. (2023a) and Fujita et al. (2023b), who studied the correlation between the jet power estimated from X-ray cavities (P_{cav}) and the molecular gas mass within 500 pc in a sample of massive elliptical galaxies. This difference in results could be explained by the sample studied by these two works. In these works they study 9 and 13 objects respectively which is significantly smaller than the 35 objects used in our work. They also look for correlations exclusively in elliptical galaxies compared to diverse range of galaxies and activities types study in our work.

Overall, the lack of correlation between the circumnuclear molecular gas mass and radio emission in our sample may suggest that jets are not directly powered by accretion from circumnuclear gas reservoirs, or that such correlation only exists over very long time-scales. As discussed earlier, the dynamical times at the spatial scales probed here are still long compared to most AGN lifetime estimates. While radio jets can extend on large scales (and thus allow us to average AGN activity over longer time-scales than direct tracers such as X-ray emission), this time-scale mismatch may be too large to lead to any strong correlation.

5.1.3 Optical line emission

As described in subsection 2.3.3, we estimated the accretion rate in our sources using also the [O III] line emission as a tracer, finding again no correlation with the molecular gas mass in the circumnuclear regions (see subsection 4.3 and Fig. 7). One could ascribe this lack of correlation to contamination from other sources of [O III] emission on larger scales (e.g. [O III] can also be a tracer of star-forming regions). This kind of contamination, however, has been found to be relevant only in higher redshift galaxies (e.g. Suzuki et al. 2016), and should therefore be minimal in nearby galaxies like our sample sources.

This result provides support to the hypotheses formulated earlier that either the level of nuclear activity in a given galaxy does not exclusively depend on the amount of cold gas around the central SMBH, or temporal variations in the accretion rate wash out any correlation. These results also support the idea that AGN fuelling mechanisms are not ubiquitous and different processes may be at play in different AGN types.

5.2 Nuclear activity and structure of the molecular gas reservoir

For a sample of nearby Seyfert galaxies, García-Burillo et al. (2021) reported that AGN luminosity (traced by 2–10 keV X-ray emission) correlates strongly with the structure of the molecular ISM (traced by CO) in the central 200 pc. This could be due to AGN feedback impacting the cold molecular gas reservoirs at these scales, and driving the molecular gas away from (and/or heating/destroying it in) the centres of the galaxies.

As discussed in – for example Davis et al. (2018), some of the WISDOM sample galaxies have central molecular gas holes, and so it is possible the same mechanism is occurring here. We test this in Fig. 8, where we plot the 2–10 keV X-ray luminosity against molecular gas concentration (as defined in Section 2) for both our sample and that of García-Burillo et al. (2021). Our galaxies span a range of X-ray luminosities and molecular gas concentrations similar

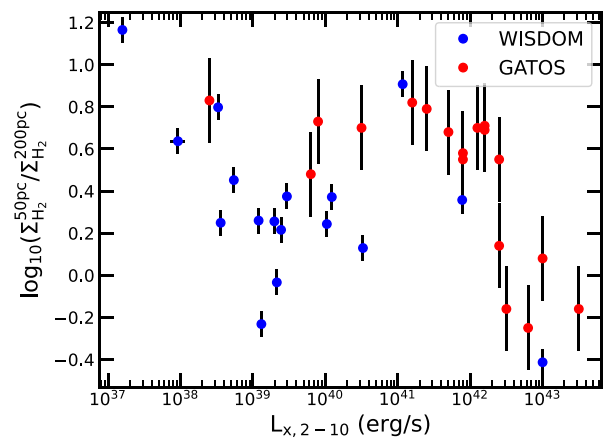


Figure 8. 2–10 keV X-ray luminosity versus nuclear molecular gas concentration. Blue data points are for the sample analysed in this work, red data points are from García-Burillo et al. (2021). The galaxies in our sample do not obey the trend reported in such previous work. This suggests that either the impact of AGN feedback is still detectable in a galaxy when it has gone into a lower activity phase, or the structure of the nuclear molecular gas is not determined by AGN processes.

to those of García-Burillo et al. (2021), but do not seem to follow the same correlation.

The lack of any correlation in our galaxy sample, which spans a wide range of AGN types and L_{bol} ($10^{41} - 10^{46} \text{ erg s}^{-1}$) and does include a significant number of Seyferts (albeit not selected to be especially active), suggests two possibilities:

(i) The central structure of the molecular gas in galaxies is set by secular (non AGN-driven) process(es). The correlation of García-Burillo et al. (2021) could then arise if these processes correlate with the SMBH-mass (or another variable SMBH-mass correlates with, such as spheroid mass/velocity dispersion), and thus the maximum AGN power possible. Some putative processes that could cause nuclear holes in the cold gas distributions (such as shear; see Davis et al. 2018) could naturally follow such a scaling.

(ii) The central structure of the molecular gas in our galaxies has been impacted by AGN feedback, but the black hole is now in a phase of lower activity. If this was the case, a galaxy would be expected to obey the García-Burillo et al. (2021) correlation until its AGN episode dies off, then decrease in X-ray luminosity while presenting its feedback-affected molecular gas structure for some time, before further inflows reset the cycle.

Comparing the WISDOM sample to the galaxies studied in García-Burillo et al. (2021), it seems that secular processes are the more likely scenario. Our sample contains more early-type hosts, but other galaxy and AGN properties are similar. It is unclear why the SMBH and its energy output (set on sub-parsec scales) would care about the large-scale galaxy properties, thus implying that the central molecular gas concentration is set by secular processes rather than by the nuclear activity. Alternatively, the parameter space explored in García-Burillo et al. (2021) could represent the turnover point between secular processes and AGN feedback, with the turnover happening at X-ray luminosities around $10^{42} \text{ erg s}^{-1}$. Our points would then fit this model with the sample AGN with X-ray luminosities lower than $10^{42} \text{ erg s}^{-1}$ and a range of molecular gas concentrations set by secular processes. The few galaxies in our sample with X-ray luminosities higher than $10^{42} \text{ erg s}^{-1}$ instead follow the relation found in García-Burillo et al. (2021). Determining

which of these possibilities is at work in our sample galaxies is interesting, but will require further observations and simulations of molecular gas at the centres of active galaxies of all luminosities. This will be explored further in future works.

6 CONCLUSIONS

We have searched for correlations between the cold molecular gas masses on the circumnuclear regions of a sample of 35 nearby galaxies and AGN activity tracers at radio, X-ray, optical, and sub-mm wavelengths. We find that the molecular gas masses of our sample sources, measured within a range of elliptical apertures with radii from 50 to 100 pc, do not correlate with any of the adopted tracers.

The sample analysed in this study includes galaxies with a range of nuclear activities and global properties, and we are unable to reproduce any of the results found for other AGN-specific subsamples. This suggests the level of nuclear activity in a given galaxy cannot purely be due the amount of cold gas fuel reservoir around the central SMBH. The fuelling mechanism of active galaxies is not ubiquitous and may vary between AGN types, and time-scale variations are likely very important.

We also probed the molecular concentration of the circumnuclear gas discs in our sample galaxies to assess whether they had been impacted by AGN feedback. There is no evidence of a relation between structure on circumnuclear scales and current accretion rate, in contrast to results found for some nearby Seyfert galaxies selected to be in an active phase and despite our objects spanning the same range in circumnuclear properties. This could indicate that these galaxies were previously in a more active phase that impacted the circumnuclear gas, or that these molecular concentrations arise naturally within circumnuclear gas discs and are not related to AGN processes.

Further observations and theoretical studies are clearly needed to make further progress to determine the link between circumnuclear gas reservoirs and nuclear activity. For instance, dense gas may be better linked to the direct reservoirs for accretion, and expanded sample sizes may help to overcome time-scale issues.

ACKNOWLEDGEMENTS

This work is supported by the UKRI AIMLAC CDT, funded by grant number EP/S023992/1. TAD and IR acknowledges support from STFC grant number ST/S00033X/1. MB was supported by STFC consolidated grant ‘Astrophysics at Oxford’ ST/H002456/1 and ST/K00106X/1. TGW acknowledges funding from the European Research Council (ERC) under the European Union’s Horizon 2020 research and innovation programme (grant agreement no. 694343). JG gratefully acknowledges financial support from the Swiss National Science Foundation (grant no. CRSII5_193826).

This research made use of ASTROPY⁵, a community-developed PYTHON package for Astronomy (Astropy Collaboration et al. 2013, 2018), MATPLOTLIB⁶, an open source visualization package (Hunter 2007), NUMPY⁷, an open source numerical computation library (Harris et al. 2020), and PANDAS⁸, a data manipulation software library (Wes McKinney 2010; pandas development team 2022).

⁵<http://www.astropy.org/>

⁶<https://matplotlib.org/>

⁷<https://numpy.org/>

⁸<https://pandas.pydata.org/>

This paper makes use of ALMA data. ALMA is a partnership of the ESO (representing its member states), NSF (USA), and NINS (Japan), together with the NRC (Canada), NSC, ASIAA (Taiwan), and KASI (Republic of Korea), in cooperation with the Republic of Chile. The Joint ALMA Observatory is operated by the ESO, AUI/NRAO, and NAOJ.

This paper has also made use of the NASA/IPAC Extragalactic Data base (NED) which is operated by the Jet Propulsion Laboratory, California Institute of Technology under contract with NASA.

7 DATA AVAILABILITY

The data underlying this article are available in the ALMA archive, at <http://almascience.eso.org/aq/>. Archival data are available from the NASA/IPAC Extragalactic Data base (NED), at <https://ned.ipac.caltech.edu/> and Dustpedia, at <http://dustpedia.astro.noa.gr/>. The data used and the final plots will be shared upon a reasonable request to the first author.

REFERENCES

- Alexander D. M., Hickox R. C., 2012, *New A Rev.*, 56, 93
 Allen S. W., Dunn R. J. H., Fabian A. C., Taylor G. B., Reynolds C. S., 2006, *MNRAS*, 372, 21
 Antonucci R., 1993, *ARA&A*, 31, 473
 Astropy Collaboration et al., 2013, *A&A*, 558, 33
 Astropy Collaboration et al., 2018, *AJ*, 156, 123
 Babyk I. V., McNamara B. R., Tamhane P. D., Nulsen P. E. J., Russell H. R., Edge A. C., 2019, *ApJ*, 887, L149
 Baldwin J. A., Phillips M. M., Terlevich R., 1981, *PASP*, 93, 5
 Balmaverde B., Baldi R. D., Capetti A., 2008, *A&A*, 486, 119
 Becker R. H., White R. L., Helfand D. J., 1994, in Crabtree D. R., Hanisch R. J., Barnes J.eds, *Astronomical Society of the Pacific Conference Series*, Vol. 61, *Astronomical Data Analysis Software and Systems III*. Astronomical Society of the Pacific., San Francisco, p. 165
 Behar E., Baldi R. D., Laor A., Horesh A., Stevens J., Tzioumis T., 2015, *MNRAS*, 451, 517
 Behar E., Vogel S., Baldi R. D., Smith K. L., Mushotzky R. F., 2018, *MNRAS*, 478, 399
 Best P. N., Heckman T. M., 2012, *MNRAS*, 421, 1569
 Bi S., Feng H., Ho L. C., 2020, *ApJ*, 900, L124
 Blundell K. M., Fabian A. C., Crawford C. S., Erlund M. C., Celotti A., 2006, *ApJ*, 644, L13
 Bolatto A. D., Wolfire M., Leroy A. K., 2013, *ARA&A*, 51, 207
 Bonatto C. J., Pastoriza M. G., 1997, *ApJ*, 486, L132
 Bondi H., 1952, *MNRAS*, 112, 195
 Boroson B., Kim D.-W., Fabbiano G., 2011, *ApJ*, 729, L12
 Bower R. G., Benson A. J., Malbon R., Helly J. C., Frenk C. S., Baugh C. M., Cole S., Lacey C. G., 2006, *MNRAS*, 370, 645
 Buttiglione S., Capetti A., Celotti A., Axon D. J., Chiaberge M., Macchetto F. D., Sparks W. B., 2009, *A&A*, 495, 1033
 Cappellari M., 2013, *ApJ*, 778, L2
 Cappellari M. et al., 2013, *MNRAS*, 432, 1862
 Cavagnolo K. W., McNamara B. R., Nulsen P. E. J., Carilli C. L., Jones C., Birzan L., 2010, *ApJ*, 720, L1066
 Ciotti L., Ostriker J. P., 1997, *ApJ*, 487, L105
 Combes F. et al., 2013, *A&A*, 558, 124
 Condon J. J., Cotton W. D., Greisen E. W., Yin Q. F., Perley R. A., Taylor G. B., Broderick J. J., 1998, *AJ*, 115, 1693
 Cook D. O., van Sistine A., Singer L., Kasliwal M. M., Kaplan D., *Iptf Collaboration*, Growth Collaboration, 2017, GRB Coordinates Network, 21707, 1
 Crawford C. S., Allen S. W., Ebeling H., Edge A. C., Fabian A. C., 1999, *MNRAS*, 306, 857
 Croton D. J. et al., 2006, *MNRAS*, 365, 11

- Davis T. A., Bureau M., Onishi K., Cappellari M., Iguchi S., Sarzi M., 2017, *MNRAS*, 468, 4675
- Davis T. A. et al., 2018, *MNRAS*, 473, 3818
- Davis T. A. et al., 2020, *MNRAS*, 496, 4061
- Davis T. A. et al., 2022, *MNRAS*, 512, 1522
- De Robertis M. M., Osterbrock D. E., 1986, *ApJ*, 301, L727
- Doi A., Inoue Y., 2016, *PASJ*, 68, 56
- Ferrarese L., Merritt D., 2000, *ApJ*, 539, L9
- Fujita Y., Izumi T., Kawakatu N., Nagai H., Hirasawa R., Ikeda Y., 2023a, *PASJ*, 75, 925
- Fujita Y., Izumi T., Nagai H., Kawakatu N., Kawanaka N., 2023b, preprint (arXiv:2310.03794)
- Galeev A. A., Rosner R., Vaiana G. S., 1979, *ApJ*, 229, L318
- García-Burillo S. et al., 2014, *A&A*, 567, 125
- García-Burillo S. et al., 2021, *A&A*, 652, 98
- Gaspari M., Ruzsokowski M., Oh S. P., 2013, *MNRAS*, 432, 3401
- Gaspari M., Brighenti F., Temi P., 2015, *A&A*, 579, 62
- Gaspari M., Temi P., Brighenti F., 2017, *MNRAS*, 466, 677
- Gleisinger R. C., O’Dea C. P., Gallimore J. F., Wykes S., Baum S. A., 2020, *ApJ*, 905, L42
- Grimm H. J., Gilfanov M., Sunyaev R., 2003, *MNRAS*, 339, 793
- Gültekin K. et al., 2009, *ApJ*, 698, L198
- Hardcastle M. J., Evans D. A., Croston J. H., 2007, *MNRAS*, 376, 1849
- Harris C. R. et al., 2020, *Nature*, 585, 357
- Harrison C. M., 2017, *Nature Astron.*, 1, 0165
- Heckman T. M., Best P. N., 2014, *ARA&A*, 52, 589
- Heckman T. M., Kauffmann G., Brinchmann J., Charlot S., Tremonti C., White S. D. M., 2004, *ApJ*, 613, L109
- Ho L. C., 2008, *ARA&A*, 46, 475
- Ho L. C., Filippenko A. V., Sargent W. L., 1995, *ApJS*, 98, 477
- Hunter J. D., 2007, *Comput. Sci. Eng.*, 9, 90
- Izumi T., Kawakatu N., Kohno K., 2016, *ApJ*, 827, L81
- Jarrett T. H., Chester T., Cutri R., Schneider S. E., Huchra J. P., 2003, *AJ*, 125, 525
- Jiménez-Donaire M. J. et al., 2019, *ApJ*, 880, L127
- Kawamuro T. et al., 2022, *ApJ*, 938, L87
- Kewley L. J., Groves B., Kauffmann G., Heckman T., 2006, *MNRAS*, 372, 961
- Kim D.-W., Fabbiano G., 2004, *ApJ*, 611, L846
- King A., Nixon C., 2015, *MNRAS*, 453, 46
- King A., Pounds K., 2015, *ARA&A*, 53, 115
- King A. R., Pringle J. E., 2007, *MNRAS*, 377, 25
- Komissarov S. S., Gubanov A. G., 1994, *A&A*, 285, 27
- Kormendy J., Ho L. C., 2013, *ARA&A*, 51, 511
- Koss M. J. et al., 2021, *ApJS*, 252, 29
- Laing R. A., Bridle A. H., 2013, *MNRAS*, 432, 1114
- Lelli F., Davis T. A., Bureau M., Cappellari M., Liu L., Ruffa I., Smith M. D., Williams T. G., 2022, *MNRAS*, 516, 4066
- Leroy A. K., Walter F., Brinks E., Bigiel F., de Blok W. J. G., Madore B., Thornley M. D., 2008, *AJ*, 136, 2782
- Leroy A. K. et al., 2019, *ApJS*, 244, 24
- Leroy A. K. et al., 2022, *ApJ*, 927, L149
- Liu Y., Jiang D. R., Gu M. F., 2006, *ApJ*, 637, L669
- Maccagni F. M. et al., 2023, *A&A*, 675, 59
- Magorrian J. et al., 1998, *AJ*, 115, 2285
- Marconi A., Hunt L. K., 2003, *ApJ*, 589, L21
- Marconi A., Risaliti G., Gilli R., Hunt L. K., Maiolino R., Salvati M., 2004, *MNRAS*, 351, 169
- Martini P., Regan M. W., Mulchaey J. S., Pogge R. W., 2003, *ApJ*, 589, L774
- McKinney W., 2010, in van der Walt S. Millman J. eds, Proceedings of the 9th Python in Science Conference. Texas, USA, p. 56
- McMullin J. P., Waters B., Schiebel D., Young W., Golap K., 2007, in Shaw R. A., Hill F., Bell D. J. eds, Astronomical Society of the Pacific Conference Series, Vol. 376, Astronomical Data Analysis Software and Systems XVI. Astron. Soc. Pac., San Francisco, p. 127
- McNamara B. R., Russell H. R., Nulsen P. E. J., Hogan M. T., Fabian A. C., Pulido F., Edge A. C., 2016, *ApJ*, 830, L79
- Molina J., Shangguan J., Wang R., Ho L. C., Bauer F. E., Treister E., 2023, *ApJ*, 950, 60
- Morganti R., 2017, *Front. astron. space sci.*, 4, 42
- Moustakas J., Kennicutt Robert C. J., Tremonti C. A., Dale D. A., Smith J.-D. T., Calzetti D., 2010, *ApJS*, 190, 233
- Murphy E. J. et al., 2011, *ApJ*, 737, L67
- Narayan R., Yi I., 1995, *ApJ*, 452, L710
- Nayakshin S., Power C., King A. R., 2012, *ApJ*, 753, L15
- Negri A., Posacki S., Pellegrini S., Ciotti L., 2014, *MNRAS*, 445, 1351
- North E. V. et al., 2019, *MNRAS*, 490, 319
- North E. V. et al., 2021, *MNRAS*, 503, 5179
- Ocaña Flaquer B., Leon S., Combes F., Lim J., 2010, *A&A*, 518, 9
- Onishi K., Iguchi S., Davis T. A., Bureau M., Cappellari M., Sarzi M., Blitz L., 2017, *MNRAS*, 468, 4663
- Pizzolato F., Soker N., 2005, *ApJ*, 632, L821
- Pizzolato F., Soker N., 2010, *MNRAS*, 408, 961
- Prandoni I., Laing R. A., de Ruiter H. R., Parma P., 2010, *A&A*, 523, 38
- Pandas development team T., 2022, pandas-dev/pandas: Pandas. <https://doi.org/10.5281/zenodo.7093122>
- Reeves J. N., Turner M. J. L., 2000, *MNRAS*, 316, 234
- Rodríguez-Ardila A., Pastoriza M. G., Donzelli C. J., 2000, *ApJS*, 126, 63
- Rosario D. J. et al., 2018, *MNRAS*, 473, 5658
- Ruffa I. et al., 2019a, *MNRAS*, 484, 4239
- Ruffa I. et al., 2019b, *MNRAS*, 489, 3739
- Ruffa I., Laing R. A., Prandoni I., Paladino R., Parma P., Davis T. A., Bureau M., 2020, *MNRAS*, 499, 5719
- Ruffa I., Prandoni I., Davis T. A., Laing R. A., Paladino R., Casasola V., Parma P., Bureau M., 2022, *MNRAS*, 510, 4485
- Ruffa I. et al., 2024, *MNRASL*, 528, L76
- Ruffa I. et al., 2023b, *MNRAS*, 522, 6170
- Sandstrom K. M. et al., 2013, *ApJ*, 777, L5
- Seth A. C. et al., 2010, *ApJ*, 714, L713
- Shakura N. I., Sunyaev R. A., 1973, *A&A*, 24, 337
- Shlosman I., Frank J., Begelman M. C., 1989, *Nature*, 338, 45
- Smith M. D. et al., 2019, *MNRAS*, 485, 4359
- Smith M. D. et al., 2021a, *MNRAS*, 500, 1933
- Smith M. D. et al., 2021b, *MNRAS*, 503, 5984
- Strong A. W. et al., 1988, *A&A*, 207, 1
- Suzuki T. L. et al., 2016, *MNRAS*, 462, 181
- Tadhunter C. N., Morganti R., di Serego Alighieri S., Fosbury R. A. E., Danziger I. J., 1993, *MNRAS*, 263, 999
- Tremaine S. et al., 2002, *ApJ*, 574, L740
- Urry C. M., Padovani P., 1995, *PASP*, 107, 803
- Veale M., Ma C.-P., Greene J. E., Thomas J., Blakeslee J. P., McConnell N., Walsh J. L., Ito J., 2017, *MNRAS*, 471, 1428
- Wada K., Papadopoulos P. P., Spaans M., 2009, *ApJ*, 702, L63
- Wagner A. Y., Bicknell G. V., Umemura M., 2012, *ApJ*, 757, L136
- Ward S. R., Harrison C. M., Costa T., Mainieri V., 2022, *MNRAS*, 514, 2936
- Wu Q., Feng J., Fan X., 2018, *ApJ*, 855, L46
- Zhu G., Zaw I., Blanton M. R., Greenhill L. J., 2011, *ApJ*, 742, L73

APPENDIX A: EMISSION DATA AND DERIVED VALUES

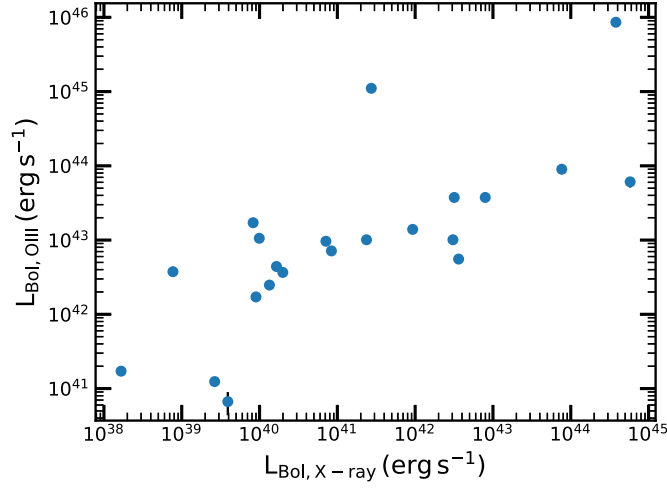


Figure A1. L_{Bol} derived from X-ray versus L_{Bol} derived from [O III].

Table A1. Emission data.

Galaxy	$L_{1.4}$	$\Delta L_{1.4}$	$E_{1.4}$	$\Delta E_{1.4}$	$L_{X, 2-10}$	$\Delta L_{X, 2-10}$	X-ray Source	L_{mm}	ΔL_{mm}	$\log_{10} \left(\frac{L_{[\text{OIII}]}}{\text{erg s}^{-1}} \right)$	$\log_{10} \left(\frac{\Delta L_{[\text{OIII}]}}{\text{erg s}^{-1}} \right)$	K_s	ΔK_s
(1)	(2)	(3)	(4)	(5)	(6)	(7)	(8)	(9)	(10)	(11)	(12)	(13)	(14)
FRL49	9.06E + 38	9.06E + 37	0.90	0.205	1.85E + 43	1.85E + 42	Chandra	1.92E + 39	7.85E + 37	42.39	0.04	9.8	0.0100
FRL1146	–	–	–	–	2.58E + 43	2.58E + 42	XMM	2.44E + 39	1.41E + 38	40.24	0.07	11	0.00800
MRK567	7.48E + 38	7.91E + 37	0.29	0.205	–	–	–	5.84E + 38	–	–	–	11	0.0450
NGC0383	3.59E + 40	3.59E + 39	3.3	0.205	3.31E + 40	3.31E + 39	Chandra	7.86E + 40	1.26E + 38	39.46	0.04	10	0.00700
NGC0404	5.36E + 34	6.99E + 33	0.49	0.227	1.58E + 37	1.58E + 36	Chandra	9.76E + 35	3.08E + 34	37.69	0.04	10	0.00700
NGC0449	5.55E + 38	5.78E + 37	0.27	0.205	3.78E + 40	3.78E + 39	XMM	7.47E + 38	3.05E + 37	41.50	0.04	12	0.0230
NGC0524	2.80E + 36	4.61E + 35	−0.27	0.212	3.59E + 38	3.59E + 37	Chandra	8.81E + 38	3.56E + 36	37.55	0.04	10	0.0730
NGC0612	1.46E + 41	1.47E + 40	3.0	0.205	7.76E + 41	7.76E + 40	Chandra	1.19E + 41	2.84E + 38	40.03	0.04	9.9	0.0990
NGC0708	3.72E + 38	3.72E + 37	1.6	0.205	2.45E + 39	2.45E + 38	Chandra	1.27E + 39	1.58E + 37	39.10	0.04	12	0.0600
NGC1194	1.18E + 37	1.18E + 36	1.5	0.871	3.50E + 41	3.50E + 40	XMM	1.23E + 39	2.22E + 37	40.03	0.04	11	0.0320
NGC1387	2.64E + 36	4.22E + 35	−0.18	0.212	2.14E + 39	2.14E + 38	Chandra	1.17E + 38	6.03E + 36	–	–	10	0.111
NGC1574	–	–	–	–	–	–	–	3.52E + 38	3.50E + 36	–	–	10	0.0980
NGC2110	6.34E + 38	6.76E + 37	–	–	5.13E + 42	5.13E + 41	Chandra	7.72E + 39	1.64E + 38	40.41	0.04	10	0.0580
NGC3169	5.43E + 37	5.43E + 36	0.16	0.205	3.39E + 41	3.39E + 40	Chandra	3.42E + 38	1.07E + 37	39.46	0.04	10	0.0920
NGC3351	7.08E + 36	7.08E + 35	–	–	5.46E + 38	5.67E + 37	ROSAT	1.81E + 37	–	37.28	0.15	9.0	0.0150
NGC3368	1.52E + 37	1.52E + 36	0.19	0.205	1.98E + 39	1.98E + 38	ASCA	5.40E + 37	–	38.85	0.04	9.5	0.0680
NGC3607	5.67E + 36	6.57E + 35	0.010	0.206	1.45E + 39	1.45E + 38	Chandra	3.79E + 38	2.31E + 37	39.48	0.04	9.5	0.0420
NGC3862	8.13E + 40	8.13E + 39	–	–	3.92E + 41	3.92E + 40	Chandra	1.52E + 41	3.43E + 39	39.20	0.04	11	0.0370
NGC4061	5.70E + 39	5.70E + 38	3.2	0.205	–	–	–	5.98E + 39	4.46E + 38	–	–	11	0.0400
NGC4261	3.74E + 40	4.12E + 39	–	–	1.17E + 41	1.17E + 40	Chandra	6.28E + 40	4.43E + 38	39.60	0.04	9.0	0.0150
NGC4429	4.59E + 34	2.30E + 35	−1.8	2.18	1.31E + 39	1.31E + 38	Einstein	1.23E + 38	9.42E + 36	38.69	0.04	10	0.0650
NGC4435	2.72E + 36	2.72E + 36	−0.010	0.478	2.95E + 39	2.95E + 38	Chandra	5.69E + 37	1.92E + 36	39.02	0.04	10	0.0590
NGC4438	2.87E + 37	2.87E + 36	0.48	0.205	1.20E + 39	1.20E + 38	Chandra	4.08E + 37	9.81E + 36	39.69	0.04	8.8	0.0150
NGC4501	9.05E + 37	9.05E + 36	0.25	0.205	1.23E + 40	1.23E + 39	Chandra	8.01E + 37	4.39E + 36	39.31	0.04	9.0	0.0150
NGC4697	1.30E + 35	1.08E + 35	−1.1	0.413	3.31E + 38	3.31E + 37	Chandra	1.79E + 37	1.65E + 36	–	–	9.7	0.0660
NGC4826	9.30E + 36	9.03E + 35	0.40	0.204	9.23E + 37	2.05E + 37	Chandra	8.27E + 36	1.64E + 36	39.03	0.04	8.0	0.0150
NGC5064	1.93E + 38	1.93E + 37	0.89	0.205	–	–	–	9.19E + 37	8.53E + 36	–	–	11	0.0730
NGC5765b	5.03E + 38	5.03E + 37	−0.010	0.205	5.37E + 40	5.37E + 39	Chandra	1.15E + 39	2.17E + 38	–	–	10.9	0.0700
NGC5806	1.17E + 37	1.17E + 36	−0.18	0.205	–	–	–	1.85E + 37	–	–	–	11	0.0730
NGC5995	5.91E + 38	6.36E + 37	–	–	2.45E + 43	2.45E + 42	Chandra	3.22E + 39	1.07E + 38	–	–	10	0.0390
NGC6753	3.23E + 38	3.53E + 37	0.91	0.205	–	–	–	6.73E + 37	–	–	–	11	0.0990
NGC6958	2.34E + 37	2.81E + 36	0.67	0.207	–	–	–	2.92E + 39	1.51E + 37	–	–	10	0.0600
NGC7052	9.21E + 38	9.30E + 37	1.8	0.205	1.05E + 40	1.05E + 39	Chandra	1.35E + 40	6.23E + 37	39.44	0.04	11	0.0420
NGC7172	7.20E + 37	7.66E + 36	0.20	0.205	1.00E + 43	1.00E + 42	Chandra	2.74E + 39	1.04E + 38	–	–	10	0.0560
PGC043387	–	–	–	–	–	–	–	8.02E + 38	–	–	–	10.7	0.0110

Notes: (1) Galaxy name, (2) 1.4 GHz luminosity, (3) 1.4 GHz luminosity uncertainty, (4) excess radio fraction, (5) excess radio fraction uncertainty, (6) 2–10 keV X-ray luminosity, (7) (2–10) keV X-ray luminosity uncertainty, (8) the telescope used for the X-ray observation, (9) nuclear mm luminosity, (10) nuclear mm luminosity uncertainty, (11) [O III] luminosity, (12) [O III] luminosity uncertainty, (13) K_s -band magnitude, (14) K_s -band magnitude uncertainty.

Table A2. Derived quantities.

Galaxy	$\dot{M}_{X\text{-ray,acc}}$ ($M_{\odot} \text{ yr}^{-1}$)	$\Delta \dot{M}_{X\text{-ray,acc}}$ ($M_{\odot} \text{ yr}^{-1}$)	$\dot{M}_{[\text{O III}],acc}$ ($M_{\odot} \text{ yr}^{-1}$)	$\Delta \dot{M}_{[\text{O III}],acc}$ ($M_{\odot} \text{ yr}^{-1}$)
(1)	(2)	(3)	(4)	(5)
FRL49	5.70E-02	5.70E-03	1.29E + 00	1.19E-01
FRL1146	8.70E-02	8.70E-03	9.12E-03	1.47E-03
MRK567	–	–	–	–
NGC0383	3.55E-05	3.55E-06	1.51E-03	1.39E-04
NGC0404	2.50E-08	2.50E-09	2.57E-05	2.37E-06
NGC0449	4.10E-05	4.10E-06	1.66E-01	1.53E-02
NGC0524	3.98E-07	3.98E-08	1.86E-05	1.72E-06
NGC0612	1.19E-03	1.19E-04	5.63E-03	5.18E-04
NGC0708	2.48E-06	2.48E-07	6.61E-04	6.09E-05
NGC1194	4.77E-04	4.77E-05	5.63E-03	5.18E-04
NGC1387	2.17E-06	2.17E-07	–	–
NGC1574	–	–	–	–
NGC2110	1.15E-2	1.15E-3	1.91E-02	1.76E-03
NGC3169	4.60E-04	4.60E-05	1.51E-03	1.39E-04
NGC3351	5.88E-07	6.10E-08	1.00E-05	3.46E-06
NGC3368	2.01E-06	2.01E-07	3.72E-04	3.42E-05
NGC3607	1.49E-06	1.49E-07	1.59E-03	1.46E-04
NGC3862	5.43E-04	5.43E-05	8.32E-04	7.67E-05
NGC4061	–	–	–	–
NGC4261	1.39E-04	1.39E-05	2.09E-03	1.93E-04
NGC4429	1.34E-06	1.34E-07	2.57E-04	2.37E-05
NGC4435	2.98E-06	2.98E-07	5.50E-04	5.06E-05
NGC4438	1.24E-06	1.24E-07	2.57E-03	2.37E-04
NGC4501	1.26E-05	1.26E-06	1.07E-03	9.87E-05
NGC4697	3.68E-07	3.68E-08	–	–
NGC4826	1.16E-07	2.56E-08	5.63E-04	5.18E-05
NGC5064	–	–	–	–
NGC5765b	5.96E-05	5.96E-06	–	–
NGC5806	–	–	–	–
NGC5995	8.14E-02	8.14E-03	–	–
NGC6753	–	–	–	–
NGC6958	–	–	–	–
NGC7052	1.07E-05	1.07E-6	1.45E-03	1.33E-04
NGC7172	2.63E-02	2.63E-03	–	–
PGC043387	–	–	–	–

Notes: (1) Galaxy name. (2) X-ray-traced accretion rate. (3) X-ray-traced accretion rate uncertainty. (4) [O III]-traced accretion rate. (5) [O III]-traced accretion rate uncertainty.

Table A3. CO integrated intensity data.

Galaxy	I_{CO} (200 pc) (Jy km s ⁻¹)	ΔI_{CO} (Jy km s ⁻¹)	I_{CO} (100 pc) (Jy km s ⁻¹)	ΔI_{CO} (Jy km s ⁻¹)	I_{CO} (75 pc) (Jy km s ⁻¹)	ΔI_{CO} (Jy km s ⁻¹)	I_{CO} (50 pc) (Jy km s ⁻¹)	ΔI_{CO} (Jy km s ⁻¹)
(1)	(2)	(3)	(4)	(5)	(6)	(7)	(8)	(9)
FRL49	7.75	0.78	2.39	0.24	–	–	–	–
FRL1146	–	–	–	–	–	–	–	–
MRK567	9.58	0.96	3.98	0.4	–	–	–	–
NGC0383	7.60	0.76	2.74	0.27	1.6	0.16	0.64	0.06
NGC0404	39.62	3.96	39.73	3.97	39.07	3.91	36.14	3.61
NGC0449	–	–	–	–	–	–	–	–
NGC0524	11.64	1.16	3.77	0.38	2.48	0.25	1.29	0.13
NGC0612	2.22	0.22	0.58	0.06	0.44	0.05	0.32	0.04
NGC0708	9.24	0.92	3.18	0.32	2.05	0.21	0.95	0.1
NGC1194	2.58	0.26	1.13	0.11	0.76	0.08	–	–
NGC1387	27.95	2.80	6.8	0.68	3.78	0.38	1.62	0.16
NGC1574	3.98	0.40	3.53	0.35	2.89	0.29	1.6	0.16
NGC2110	4.62	0.46	1.21	0.12	–	–	–	–
NGC3169	125.84	12.58	43.18	4.32	26.99	2.7	–	–
NGC3351	104.99	10.50	55.74	5.57	32.78	3.28	18.57	1.86
NGC3368	170.74	17.07	54.79	5.48	35.54	3.55	19.23	1.92
NGC3607	37.39	3.74	15.56	1.56	10.37	1.04	–	–
NGC3862	–	–	–	–	–	–	–	–
NGC4061	1.21	0.12	0.34	0.03	0.21	0.02	–	–
NGC4261	5.91	0.59	5.49	0.55	4.59	0.46	2.98	0.3
NGC4429	17.38	1.74	3.64	0.36	2	0.2	0.64	0.06
NGC4435	35.67	3.57	15.68	1.57	9.91	0.99	5.28	0.53
NGC4438	134.20	13.42	52.63	5.26	32.86	3.29	15.26	1.53
NGC4501	137.79	13.78	63.66	6.37	40.61	4.06	20.26	2.03
NGC4697	1.90	0.19	1.55	0.16	1.23	0.12	0.74	0.07
NGC4826	276.92	27.69	193.02	19.3	148.73	14.87	74.96	7.5
NGC5064	27.91	2.79	9.7	0.97	5.27	0.53	2.58	0.26
NGC5765b	4.70	0.47	–	–	–	–	–	–
NGC5806	19.20	1.92	7.53	0.75	5.46	0.55	3.09	0.31
NGC5995	–	–	–	–	–	–	–	–
NGC6753	57.58	5.76	19.66	1.97	11.8	1.18	5.65	0.56
NGC6958	12.76	1.28	3.76	0.38	2.3	0.23	1.03	0.11
NGC7052	5.06	0.51	2.2	0.22	1.33	0.13	0.55	0.06
NGC7172	47.03	4.70	6.19	0.62	2.85	0.29	1.14	0.11
PGC043387	–	–	–	–	–	–	–	–

Notes: (1) Galaxy name. (2) 200 pc radius aperture integrated CO intensity. (3) 200 pc aperture CO intensity uncertainty. (4)–(9) Follows the same trend for the 100, 75, and 50 pc radius apertures.

Table A4. Median and KS test p -values for the samples used in this work.

	Median values for samples			
	This work	Garcia-Burillo + 21	Izumi + 16	Babyk + 19
$\log L_{\text{bol}}(\text{erg s}^{-1})$	43.2	43.0	43.3	–
$\log M_{\text{BH}}(M_{\odot})$	8.04	7.09	7.38	–
$\log(\lambda_{\text{edd}})$	–2.57	–2.20	–2.17	–
$\log P_{\text{jet}}(\text{erg s}^{-1})$	42.3	–	–	42.3
	KS test			p -values
	Samples			
	This work-GB + 21 (L_{bol})			0.015
	This work-Izumi + 16 (L_{bol})			0.001
	This work-GB + 21 (M_{BH})			0.0003
	This work-Izumi + 16 (M_{BH})			7.27×10^{-5}
	This work-GB + 21 (λ_{edd})			0.03
	This work-Izumi + 16 (λ_{edd})			0.003
	This work-Babyk + 19 (P_{jet})			0.53

This paper has been typeset from a $\text{\TeX}/\text{\LaTeX}$ file prepared by the author.